Spring 2020

Pumice Compositions and Mineral Chemistry from Lascar Volcano, Chile

Madelaine M. Stearn
Missouri State University, Madelaine119@live.missouristate.edu

PUMICE COMPOSITIONS AND MINERAL CHEMISTRY FROM LASCAR VOLCANO, CHILE

A Master's Thesis

Presented to

The Graduate College of

Missouri State University

In Partial Fulfillment

Of the Requirements for the Degree

Master of Science, Geography and Geology

By

Madelaine M. Stearn

May 2020

PUMICE COMPOSITIONS AND MINERAL CHEMISTRY FROM LASCAR VOLCANO, CHILE

Geography, Geology, and Planning

Missouri State University, May 2020

Master of Science

Madelaine M. Stearn

ABSTRACT

Lascar volcano is one the most active volcano in the Central Volcanic Zone of the Andean Cordillera, with 36 Holocene eruptions including a VEI 4 eruption in April 1993. Activity has not been consistent throughout time, and therefore, the processes behind it are poorly understood. Lascar volcano has cyclic behavior and has had four stages of activity, each of which had a unique eruptive style and product composition. Stage I (<43 ka) had primarily mafic andesite lavas erupted effusively from a stratocone. Stage II initiated with dome building events ESE of the original vent and culminated in the 26.45 ka Soncor deposit, which is the largest ignimbrite erupted from Lascar. After the Soncor ignimbrite, there was then a period of quiescence, ending with the Tumbres pyroclastic flow (9.2 ka) and Tumbres-Talabre lava (7.1 ka) deposits defining Stage III. The current Stage IV eruptions are Vulcanian to Plinian and produce lava domes, pyroclastic flows, and pumices. The aim of this project is to determine if the bimodal nature of the pumices is caused by rejuvenation of magma into Lascar's reservoir via diffusion geochronometry of zircon, geochemistry of plagioclase, and petrography of samples. If so, that would explain the cyclic nature and dynamic compositions that Lascar exhibits. The paucity of zircon prevents geochronological study at this time, and results for age dating were inconclusive. However, plagioclase data from other methods suggests that Lascar is not sourced from the Altiplano Puna Magma Body; a model of multiple smaller mama chambers at a variety of depths matches more closely. Additionally, data supports a bimodal chamber in which magma mixing is a core mechanism in differentiation in the system. Geothermobarometry of pyroxenes and plagioclase suggest an average magma chamber depth of approximately 6km.

KEYWORDS: volcanology, geology, mineralogy, geochemistry, plagioclase

PUMICE COMPOSITIONS AND MINERAL CHEMISTRY FROM LASCAR VOLCANO, CHILE

By

Madelaine M. Stearn

A Master's Thesis
Submitted to the Graduate College
Of Missouri State University
In Partial Fulfillment of the Requirements
For the Degree of Master of Science, Geography and Geology

May 2020

Approved:

Gary Michelfelder, Ph.D., Thesis Committee Chair

Matthew McKay, Ph.D., Committee Member

Charles Rovey, Ph.D., Committee Member

Julie Masterson, Ph.D., Dean of the Graduate College

ACKNOWLEDGEMENTS

I would like to thank the following people for their support during the course of my graduate studies: my advisor Gary Michelfelder for providing me with the opportunity to complete this project this project, and for his guidance throughout the process. I would also like to thank Dr. Charles Rovey and Dr. Matthew McKay for being on my committee and offering valuable assistance. Thank you to Missouri State University for creating an atmosphere of success, and my graduate student colleagues for their support. I could not have finished this without the help and encouragement of all of these people.

TABLE OF CONTENTS

LIST OF TABLES

LIST OF FIGURES

INTRODUCTION

Long-lived, melt dominated magma reservoirs with simple geometries have been the basis for models of volcanic systems and eruption dynamics. In the past two decades our understanding of magmatic processes through the use of microanalytical techniques and magma plumbing systems through geophysical and petrologic investigations have refined our understanding and ability to track magmatic processes at scales which provide insight into the various source components of arc magmatism (Davidson et al., 2007; Ginibre and Davidson, 2014; Caracciolo et al., 2020). Magma storage systems beneath active volcanoes are now modeled to be sets of crustal reservoirs that are composed of a series of liquid-poor mushes (Marsh, 2006; Annen, 2009; Ward et al., 2017; Pritchard et al., 2018; Edmonds et al., 2019) with isolated frameworks of melt separate from the remainder of the reservoir (Bégué et al., 2014; Cooper and Kent, 2014; Gelman et al., 2014; Bergantz et al., 2015; Bachmann and Huber, 2016; Cooper, 2017). Various models have been discussed to explain the variability, origin, and extraction of these melts ranging from rapid remobilization of cold mushes (Cooper and Kent, 2014) to warm storage crystal segregation from the mush (Gualda et al., 2018). Plagioclase is useful in recording these processes due to the preservation of major element variations in the phases and sensitivity to small-scale system changes in pressure, temperature, and system compositional variation (Davidson et al., 2007; Ginibre et al., 2007; Ginibre and Davidson, 2014).

Lascar volcano, a composite cone in the Altiplano of northern Chile, is arguably the most active arc volcano in the Andean Central Volcanic Zone (CVZ), with a VEI 4 subplinian eruption in April of 1993 and 10 smaller eruptions between 1994 and 2015 (de Zeeuw-van

Dalfsen et al., 2017). The modern volcanic complex consists of a western edifice and the active eastern edifice comprised of three overlapping craters (de Zeeuw-van Dalfsen et al., 2017). The geographic location of Lascar is of significant scientific interest and has been included in recent geophysical studies of the Altiplano-Puna Magma Body (APMB) and other geodetic observation of volcanic deformation within the CVZ (Henderson and Pritchard, 2013). The modern arc of the CVZ is constructed along the southernmost limits of the Altiplano-Puna Volcanic Complex (APVC) at the seismically inferred southern boundary of the APMB (Burns et al., 2015; Díaz et al., 2015; Fig.1). Unlike other volcanic centers with surface deformation within these boundaries, Lascar exhibits cyclic behavior and has had four distinct stages of activity, with each stage producing material of unique composition (Gardeweg et al., 1998). Despite its active nature and cyclic behavior, there has been little investigation into Lascar in the last decade, most likely due to its location in a remote and hard to access area. Previous research on Lascar has determined the volcanic stratigraphy, petrological analyses of individual eruptive events (Matthews et al., 1994, 1999) and descriptions of the evolution and geometry of the magma chamber (Gardeweg et al., 1998). The most recent work has focused on geophysical studies (e.g. Pavez et al., 2006; Díaz et al., 2012), LiDAR and other aerial imaging (Oppenheimer et al., 1993), but the geometry and architecture of the magma plumbing system have largely gone unstudied. In this study I investigate the composition of pumice from three stages in Lascar's volcanic history: the Soncor ignimbrite, Tumbres pyroclastic deposit, and the 1993 VEI 4 eruption. I employ these data to determine the architecture of the magma plumbing system and the processes controlling magma evolution by comparing mineral chemistry and mineral textures, focusing on plagioclase and pyroxene, as they are useful in tracing changes in the magmas from which they resided and grew. I use calibrated X-ray maps of plagioclase to obtain distribution and abundances and petrologic

models to constrain crystallization conditions. The pumices record the pre-eruptive conditions and processes that suggest banded pumices are the product of mixing of magma and crystal populations with only minor changes in bulk composition that results from mingling between two reservoirs and recharge of hotter, slightly more mafic magma. These conclusions are supported by textural and mineralogical differences as a result of residence times within magma reservoirs isolated from the local regional magma body, the APMB.

Figure 1. Map of the Andean Central Volcanic Zone. Inset map shows the location of the CVZ within South America. Lascar, located in Chile, is highlighted in red. Modern CVZ arc front volcanoes are shown as gray triangles with the Aucanquilcha Volcanic complex in blue, and the Uturuncu volcanic complex in green. Lascar volcano is geographically located within the boundary of the APVC and on the edge of the geophysical determined boundary of the APMB (de Silva, 1989; Ward et al., 2017). The large gray area represents continental crust that is thicker than 60 km.

GEOLOGIC BACKGROUND

The Andean Cordillera is a 7,500 km mountain chain on the western margin of South America, resulting from the subduction of the oceanic Nazca plate beneath the more buoyant South American continental plate (Mamani et al., 2008). Modern subduction of the Nazca plate is one of the most rapidly subducting tectonic plates at about 63-75 mm/yr, though the peak might have been above 150 mm/yr (Kendrick et al., 2003). The Nazca plate is segmented in such a way that some areas are horizontal, whereas others are dipping at 30º (Allmendinger et al., 1997). These differences in subduction angle result in magmatism only occurring in discrete sections of steep subduction. The transitions between steeper and shallow subduction angle are very stark and caused by the modern interactions of the two plates and the inhomogeneity in the South American plate. The Nazca plate has steep subduction in four different areas, which are defined as individual zones of volcanism: the Northern Volcanic Zone, Central Volcanic Zone, Southern Volcanic Zone, and Austral Volcanic Zone (Mattioli et al., 2006). These zones are separated by areas without volcanism where segments of the Nazca plate are nearly horizontal (Allmendinger et al., 1997).

The Central Volcanic Zone (CVZ) is the middle segment of volcanic activity of the Central Andean mountain belt, and contains the thickest crust of any continental-oceanic convergent boundary in the world (de Silva, 1989; Beck et al., 2015; Farrell et al., 2017). The CVZ has had continuous magmatic activity for ~200 Ma with magmatism going through periods of crustal shortening and then intense periods of activity caused by ignimbrite flare-ups (Coira et al., 1982; Rogers and Hawkesworth, 1989; Allmendinger et al., 1997). Volcanic products from the CVZ have compositions that are much more evolved than from the other volcanic zones in the Andes, with much more crustal contamination (Harmon et al., 1984). This has produced more

than 20 calderas in the area along with approximately 50 active or recently active andesite to dacite stratovolcanoes (De Silva et al., 2006; Michelfelder et al., 2013). The CVZ consists primarily of ignimbrite deposits. These tend to be easily eroded, but the hyper-arid climate of the Central Andes has preserved much of the volcanic history of the area (Kern et al., 2016). These conditions result in the CVZ being one of the most extensive ignimbrite provinces in the world (de Silva, 1989).

Lascar volcano is the most active volcano in the Central Volcanic Zone with 36 Holocene eruptions and a VEI 4 subplinian event in April 1993 (Pavez et al., 2006; Siebert and Simkin, 2012). Current activity consists of persistent fumaroles (Tassi et al., 2009; González et al., 2015), a satellite thermal anomaly (Jay et al., 2013; Pritchard et al., 2014) and regular earthquakes and tremors since 1994 (Pritchard et al., 2014). Two cones make up the main edifice that are broken into five craters, with the central crater currently active (Gardeweg et al., 1998; Gonzales et al., 2015). The series of five nested craters oriented ENE-WSW formed from migration of the eruptive vent. The Lascar system generally produces ignimbrite and lavas in addition to scoria and bombs. Major rock types are porphyritic andesites and dacites with plagioclase phenocrysts (Matthews et al., 1994). Mafic andesites contain phenocrysts of olivine, orthopyroxene and clinopyroxene, while the silicic dacites contain phenocrysts of orthopyroxene and clinopyroxene, though some units contain phenocrysts of hornblende and biotite (Gardeweg et al., 1998). The development of Lascar is broken into four distinct stages of dome growth and eruption, with activity dating back approximately 43 ka (Table 1.).

Table 1. Stratigraphic order and pertinent data of Lascar's stages and the units within.

Unit	Description	Eruption Type	SiO_2 wt%	Age
Holocene	Compositionally banded Pumice fall and flow deposits	Vulcanian, explosive	60.2	>1848
Stage IV Lavas	Andesite lava	Effusive	-	<7.1 ka
Tumbres-Talabre	Ignimbrite and andesite lava	Pyroclastic flow	58.5	7.1 ka
Tumbres	Bands of pumice and scoria	Plinian	59.6	9.2 ka
Western Stratocone	Andesite lava	Effusive	~58.0	19.2 - 9.2 ka
Capricorn Lavas	Banded crystalline dacite lava	Effusive	63.4	19.2 - 9.2 ka
Soncor	Non-welded, compositionally zoned ignimbrite fans overlain by plinian pumice	Plinian	58.0 - 67.3	26.5 ka
Piedras Grandes	Hornblende andesite ignimbrite	Lava dome collapse	60 - 64	>26.5 ka
Chaile	Divided into Upper and Lower units; coarse-grained andesite	Pyroclastic flow	-	>26.5 ka
Saltar	Clast-supported, coarse-grained pyroclastic flow with andesite bombs	Pyroclastic flow	-	>26.5 ka
Stage I Block and Ash	Mafic andesite lavas; dome blocks	Effusive	60.3-61.4	<43.0 ka

Stage I. Activity at Lascar began with the building of an andesitic stratocone that produced three notable blocky two-pyroxene pyroclastic flow deposits. Most notable is the >26.5 ka Saltar deposit, which is a coarse-grained pyroclastic flow with large red cauliform andesite bombs within a poorly sorted ashy scoria matrix that is clast supported (Gardeweg et al., 1998). The Saltar deposit has nine distinct flow units. However, the majority of lavas from Stage I are amygdule andesites with plagioclase phenocrysts and glassy zeolites infilling vesicles.

The Upper and Lower Chaile deposits are two coarse-grained andesite pyroclastic flows (Gardeweg et al., 1998). The Lower Chaile deposit is extremely coarse grained and is clast supported with a similar matrix to the Saltar ignimbrite and pyroclastic bombs. However, Chaile bombs are rounded and denser than the Saltar bombs and in some areas, there are clasts of breccias. The Upper Chaile unit fills in topography of the Lower Chaile and is a dark gray

matrix-supported andesitic flow with much smaller scoria that possesses dacite xenoliths (Matthews et al., 1994).

Stage II. Stage II began with a transition of activity to a western crater that formed a silicic andesite and dacite lava dome complex. The major products of this stage are the Piedras Grandes (>26.5 ka) and Soncor (26.5 ka) deposits. The Piedras Grandes unit is an andesitic ignimbrite deposit that is pink to gray in color formed from dome-collapse events (Matthews et al., 1999). The unit is composed primarily of a silicic hornblende andesite with minor bands of basaltic andesite and inclusions. A second form of the Piedras Grandes is a catastrophic flood deposit, or *jokulhlaup*, consisting of thin fluvial layers of gravels and coarse sands (Gardeweg et al., 1998).

The Soncor ignimbrite is from the biggest eruption produced by Lascar, which is separated into two different units: a Plinian pumice deposit and an overlying flow deposit. The pumice deposit is a white compositionally heterogeneous andesite-dacite pumice that ranges in composition from a light silicic dacite to a darker andesitic pumice (Matthews et al., 1999). The two pumices are commonly compositionally banded.

The overlying ignimbrite is a coarse grained, non-welded, compositionally zoned flow with many distinct units. The older units consist exclusively of the white pumice, but the composition changes throughout the deposit. Younger units have pumices that range from dacites to mafic andesites, with many pumices having compositional banding. Both the Plinian pumice deposit and the ignimbrite deposit are normally zoned and layered on top of one another, with a compositional reversal occurring at the point where the two meet; this is known as double zoning (Matthews et al., 1999).

Following Stage II are two different geomorphic events: first, a debris avalanche at 22.3 ka, and second, a glaciofluvial fan (Gardeweg et al., 1998). Overlying the Soncor ignimbrite on the western flanks of Lascar is a 50 m thick debris avalanche deposit that extends 25 km out from the cone. Most of this deposit consists of large blocks of Stage I lavas in a massive white ash matrix. The glaciofluvial fan consists of alluvial and laharic gravels sourced from Stage I and Soncor deposits and is dated between 20.1 ka and 12.5 ka. This suggests ample time for erosion before the beginning of Stage III; this is interpreted as a period of quiescence from 14 ka to 10.5 ka.

Stage III. Activity restarted on the western side of Lascar with the formation of a dacitic to andesitic stratocone over the Soncor vent (Matthews et al., 1999). Lavas in this period are porphyritic andesites to dacites and include the Capricorn flow and at least one other scoria flow deposit (Gardeweg et al., 1998). The exact timeframe of cone building for Stage III is not well known, but is between 19.2 ka after the geomorphological events from Stage II and prior to the 9.2 ka Tumbres eruption. The Tumbres eruption was originally thought to have occurred in this stage, but Matthews et al. (1999) determined that the lava flow was closer temporally and mineralogically to the products from Stage IV.

Stage IV. The stage began with the production of the 9.2 ka Tumbres-Talabre Lava (Matthews et al., 1999). This created multiple thin pumice and scoria deposits that form a hummocky topography in the area. The pumices are cream in color and contain red scoria clasts, and in some cases, the scoria is banded with white pumice streak. Following the Tumbres eruption, three deep collapse craters formed, indicating movement of the vent back to the eastern side of the complex (Gardeweg et al., 1998). Lascar remains in Stage IV, and the active crater is the deepest of these collapse craters in the middle of the complex on the eastern cone.

Holocene volcanic activity at Lascar volcano consists of lava dome growth, subsidence, and degassing. The most recent lava dome growth began in 1984 and was cyclical in behavior until April 1993, when Lascar had a VEI 4 eruption (de Zeeuw-van Dalfsen et al., 2017). Since that time, there has been intermittent activity, with 10 small Vulcanian eruptions between 2013 and 2015. A total of 36 Holocene eruptions have been documented (de Zeeuw-van Dalfsen et al., 2017). The current state of Lascar is a series of five nested calderas with the eastern cone being active and the western cone being extinct (Díaz et al., 2012).

The April 18th – 20th, 1993 eruption began on April 18th and continued until April 26th. It produced several mushroom-shaped sub-Plinian clouds which created light colored pumice flows once they collapsed (Déruelle et al., 1996). The pumice flows also contained black and white banded dacitic pumice bombs and red andesitic lava blocks from the crater walls; pieces of the andesitic lava dome were also ejected. Products from this eruption are two-pyroxene porphyritic andesites and dacite pumices that lack hornblende, despite its presence in products from Lascar's previous eruptions (Déruelle et al., 1996).

METHODS

This study uses mineral chemistry of plagioclase to create an accurate picture of the cooling system before eruption. This project tested samples from multiple phases of Lascar's history. The sample from stage II is LASC-P01 from the Soncor eruption. Stage III is represented by LASC-P02, which is a pumice from the Tumbres eruption, LASC25-T01, which are from the Tumbres-Talabres lavas, LASC24-01, LASC-100, LASC24-100, and LASC24-04, which are representative of the Western Stratocone lava flows. Stage IV samples include LASC-P03, LASC-P03A, and LASC-P03B. LASC-P03 is the light dacitic end member of the bimodal pumice from the April 1993 eruption. LASC-P03A is the banded intermediate member, and LASC-P03B is the darker more mafic endmember.

Zircon were separated by grinding samples using a rock grinder. This material was then put through sieves to separate out the smaller portions (<60). This portion was then magnetically separated using a neodymium magnet, and then a Franz magnetic separator. After this I conducted a density separation via heavy liquid separation using LST (2.85 g/mL). U-Th isotopic were ratios measured to determine these age dates.

Using standard separation procedures, ten to thirty zircons were hand-picked from three samples: LASC-P01, LASC-P02, and LASC-P03. I attempted to collect zircon from three other samples, LASC-P03A, LASC 25-01 and LASC-100. Heavy mineral separates were mounted in indium mounts, however no suitably sized (>25μm) zircon grains were found upon microanalysis. Zircon were mounted and imaged using SEM (Scanning Electron Microscope) at Stanford University to assure their composition and to determine appropriate locations for

analysis. Zircon grains were not present in the samples when analyzed, though minute crystals were separated from the lava samples after an HCl acid bath.

Thin sections were made for each sample and analyzed using standard point-count methods with the use of a petrographic microscope. Plagioclase grains were selected based on patterns used by Cooper and Kent (2014) in their plagioclase diffusion study using Nomarski differential interference contrast (NDIC) imaging along with electron backscatter imaging. Select samples were analyzed by electron microprobe at the University of Iowa. Major element compositions of plagioclase and pyroxene were conducted on four lava flows using a JOEL JXA-8230 Superprobe microanalyzer (EMPA) using five wave-length-dispersive spectrometers and eight large-format diffracting crystals following the method described in Hartsock (2019). Phenocrysts and groundmass crystals were analyzed at an accelerating voltage of 15 keV with a current of 20 nA with a five micron spot size. The run-time per point was 4.25 minutes with an on-peak dwell time of 15-30 seconds and a background dwell time of 5 seconds. Transects from core to rim were analyzed when possible in spot mode. Major element contents for plagioclase were calibrated using the Astimex mineral standard Plagioclase and were accurate to <4% for all elements other than Na_2O (6.35%) and FeO (14.57%). Pyroxenes were calibrated for clinopyroxene using the Museum of Natural History standards Ney County Cr-Augite and Kakanui Augite, and the Smithsonian Microbeam standard Johnstown Meteorite Hypersthene. The additional calibration of the EPMA was performed using San Carlos Olivine from the UI-1 standard block. Values obtained via EPMA for the San Carlos Olivine were accurate to <2% for all elements other than those in extreme low abundance such as Ca, Al and Cr. Omitting elements in extreme low abundance revealed variability (% r.s.d.) of<5% for all but Ni at 8%, showing good consistency between the analytical runs. Values for the Kakanui Augite were

accurate to <4 % for all but FeO (21%) and MnO (22%). Values for the Ney County Cr-Augite were accurate to <1% for all but TiO_2, FeO, MnO and Cr_2O_3 at 16%, 25%, 29%, and 5% respectively.

RESULTS

Petrographic analysis was conducted on seven samples with the results summarized in the Tables 2-3 and Figures 2-10. Lascar volcanic rocks are porphyritic to microporphyritic andesites and dacites with phenocrysts of plagioclase, two-pyroxenes, and hornblende. Phenocrysts vary from 28-47%, with the Soncor ignimbrite pumice being less crystal-rich than the Stage III or IV pumices. Plagioclase is the dominant phenocryst phase in the majority of felsic rocks in this study, with pyroxenes more common in mafic samples. Groundmass is generally crystalline with some samples being vitrophyric. Pumice samples are highly vesicular and have a range of hypocrystalline to holocrystalline groundmass. Ignimbrites are hypocrystalline with few vesicles.

Plagioclase major element composition from pumice samples were evaluated by EMPA analysis of core to rim transects and quantitative X-ray maps of K-Na-Ca. Plagioclase phenocrysts range from An_{35-86} and are andesine-bytownite. Pyroxene crystals are a two-pyroxene system and have augite and enstatite. Depths were calculated from pressures using an average density of crust from the Andes of 2700kg/m^2 from Henderson et al., (2013). Samples are divided by Lascar's eruptive stages and flow unit.

Stage I

Stage I samples are microporphyritic block-and-ash deposits containing phenocrysts of plagioclase, pyroxene, and brown hornblende. Groundmass consists of Fe-Ti oxides, ash, pyroxenes, plagioclase, and vesicles. Samples have a medium-gray ash matrix that is partially welded with minor vesicles. Ash can show shapes such as three-pointed "stars". Plagioclase crystals are seriate in two size populations, phenocrysts and microlites. Microlites range from

approximately 5 to 50μm and have a bladed habit. Plagioclase phenocrysts are tabular and subhedral ranging from 200 to 400μm. Phenocrysts sometimes lack distinct twinning, but display coarse-sieving textures with strong resorption surfaces and defined oscillatory zoning. Two pyroxene phases are present as phenocrysts: orthopyroxene and clinopyroxene. Orthopyroxene is present in higher abundance than clinopyroxene but is often smaller in size, not exceeding 150μm. Clinopyroxenes follow the same size trends as plagioclase but are often twinned or in glomerocrysts. Both varieties are within the groundmass at similar sizes to plagioclase microlites and are rounded in shape. Hornblende are deep brown and have ompacitic rims, with some crystals entirely altered. Crystals are seriate and range from 100 to 500μm. Fe-Ti oxides are 100μm on average, some showing polygonal crystal habit. Vesicles are present but not abundant. Glomerocrysts of plagioclase and clinopyroxene are ubiquitous throughout.

Pyroxene phenocrysts range from En_{7-77} (Fig. 2). Geothermobarometry of pyroxenes modeled both clinopyroxene and orthopyroxene temperatures and pressures, with pressures used to calculate depth in km (Fig. 3). The Stage I system has two discrete populations of depths and temperatures. Clinopyroxene temperatures have a shallower population at 2km depth and 1035°C, and a deeper population at 13km and 1061°C. Orthopyroxenes also display this trend, with a shallow population at 3km and 1055°C, and a deeper population at 21km and 1090°C.

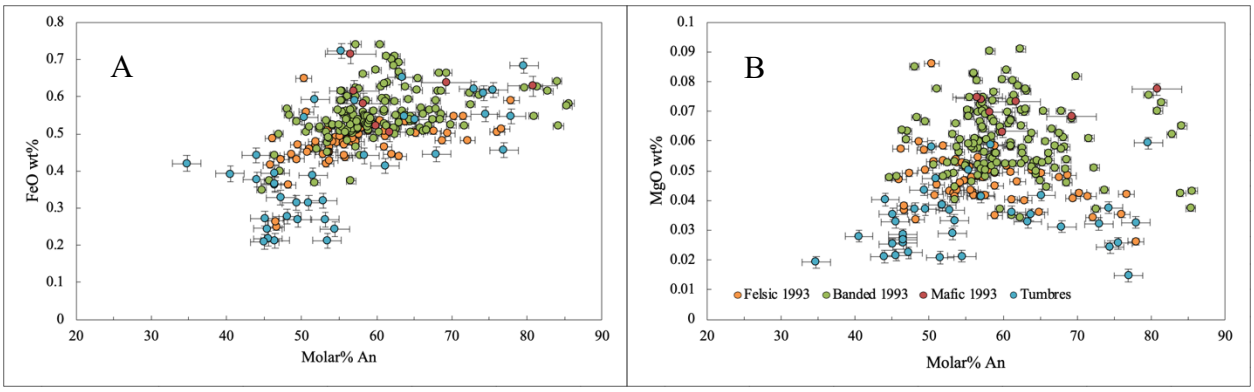

Figure 2. Molar anorthite (Molar% An) plotted against A) FeO and B) MgO weight percent. P02 shows a pattern very similar to that of P03, though slightly less metallic. P03A has a much higher wt% of metal. P03A has a composition between those two, with a robust middle section. P03B lacks data points but has consistently high values for both metals and molar anorthite. Full data can be found in Appendix A-1.

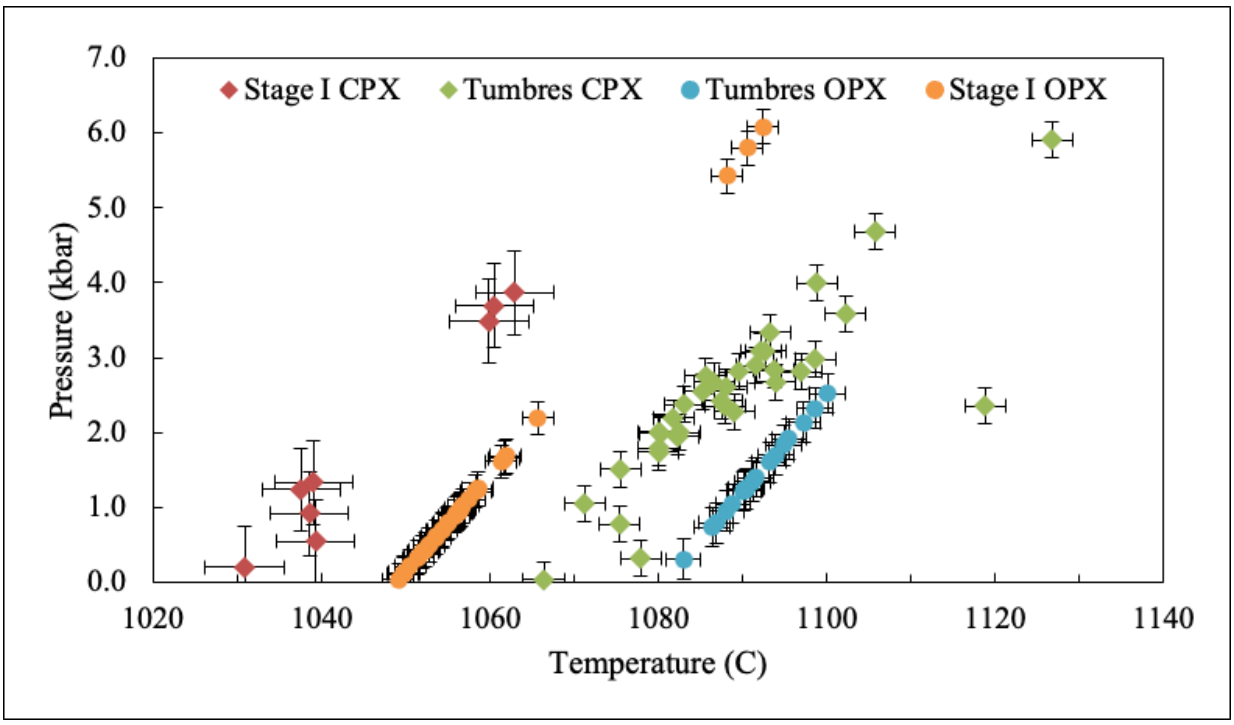

Figure 3. Temperature and pressure model of clinopyroxenes and orthopyroxenes of Stage I and Tumbres ignimbrites. Stage I lavas plot with lower temperatures than the Tumbres-Talabre lavas, averaging 1060°C for Stage I and 1091°C for Tumbres, and the orthopyroxenes plot at higher temperatures than the clinopyroxenes. Pressure data gives an average chamber depth for Tumbres at 9.1km and Stage I at 7.4km. 13 points were removed that were less than or equal to 0 at two decimal places. Pyroxene whole rock and temperature data can be found in Appendices A-2, A-3 and A-4.

Stage II

The stage II sample is a pumice from the 26.5 ka Soncor eruption. This sample is a vesicular porphyritic pumice that is tan to buff colored in hand sample. It contains two-pyroxene and plagioclase phenocrysts. Groundmass consists of Fe-Ti oxides, glass, two-pyroxenes, plagioclase, and vesicles. Plagioclase is the most abundant phenocryst in the sample, subhedral bladed to tabular and ranges in size from 400μm-2mm. Microlites and crystals in groundmass range from 5μm to 100μm with bladed habit. Pyroxenes are subhedral pale yellow-green in PPL, with orthopyroxenes generally slightly smaller in size than clinopyroxenes, ranging from 200μm to 1mm. Clinopyroxenes can be similar sizes to orthopyroxenes or plagioclase phenocrysts. Most crystals are heavily resorbed and show coarse sieving. Some show oscillatory zoning and fine sieving, though this is more abundant in the smaller phenocrysts. Pyroxenes and plagioclase form glomerocrysts, which are sparse through the sample. Groundmass consists of plagioclase, two-pyroxene, vesicles, and light beige to colorless glass.

Stage IV: Tumbres

The older two samples from Stage IV represent the 9.2ka Tumbres eruption and the >9.2ka Tumbres-Talabres eruptions. The Tumbres eruption is represented by a buff colored vesicular hypocrystalline pumice, with phenocrysts of pyroxenes and plagioclase. Pyroxenes are subhedral pale yellow-green in PPL, often with rings of glass or plagioclase on the rims. Clinopyroxene shows twinning and is less abundant than orthopyroxene. Both are heavily resorbed, some with melt inclusions, are cracked, and exist both as microlites in the groundmass and as phenocrysts. Phenocrysts average 300μm and microlites range from 30 to 100μm. Plagioclase crystals are the dominant mineral type in the sample and are also in two sizes of

phenocrysts and microlites of similar sizes to those of the pyroxenes. Plagioclase phenocrysts are subhedral, with the larger phenocrysts displaying Carlsbad and polysynthetic twinning. Many exhibit oscillatory zoning and coarse-grained sieving textures. Both pyroxenes and plagioclase can be found in glomerocrysts, as well as in xenoliths. The groundmass of the sample is mostly glass and microlites of pyroxenes and plagioclase, black in PPL and sparse Fe-Ti oxides. Vesicles are misshapen and vary in size.

Plagioclase from the pumice ranges from An_{35-80} (Fig. 2). Plagioclase types include unzoned high An, unzoned low An, oscillatory low to high An, reverse zoned, and normal zoned. High and low types are more abundant than oscillatory, normal, or reverse types. FeO wt% ranges from 0.208 to 0.723, and MgO wt% from 0.015 to 0.059. FeO averages 0.42, and MgO averages 0.034. There is a set of data with a negative trend on the higher end of the An%, and also a cluster in the lower part, from 40-55%. Transects display lower FeO values, between 0.4 and 0.5 wt% (Fig. 4). An% values are lower in the core and increase towards the rim, with core values around ~25% and increase towards 0.5 to 0.6 wt%. Chemical maps show a mix of high Ca and high Na crystals (Fig. 5). Most have a high-Ca rim, with the cores being relatively lower in Ca in the cases of anorthite crystals (P02-P2) and albite crystals also have a higher Ca rim (P02-P5). Sieving in the cores of crystals is often high in K_2O. The Tumbres sample seems to have the largest crystals being high Na, with fewer less abundant larger crystals that are higher in Ca, though both populations exist.

Samples from the Tumbres-Talabre ignimbrite are vitrophyric porphyritic ignimbrites, grayish in color with visible phenocrysts of plagioclase, pyroxenes, and hornblende. Samples have a light gray ash matrix that is continuous with few air pockets. Plagioclase crystals are

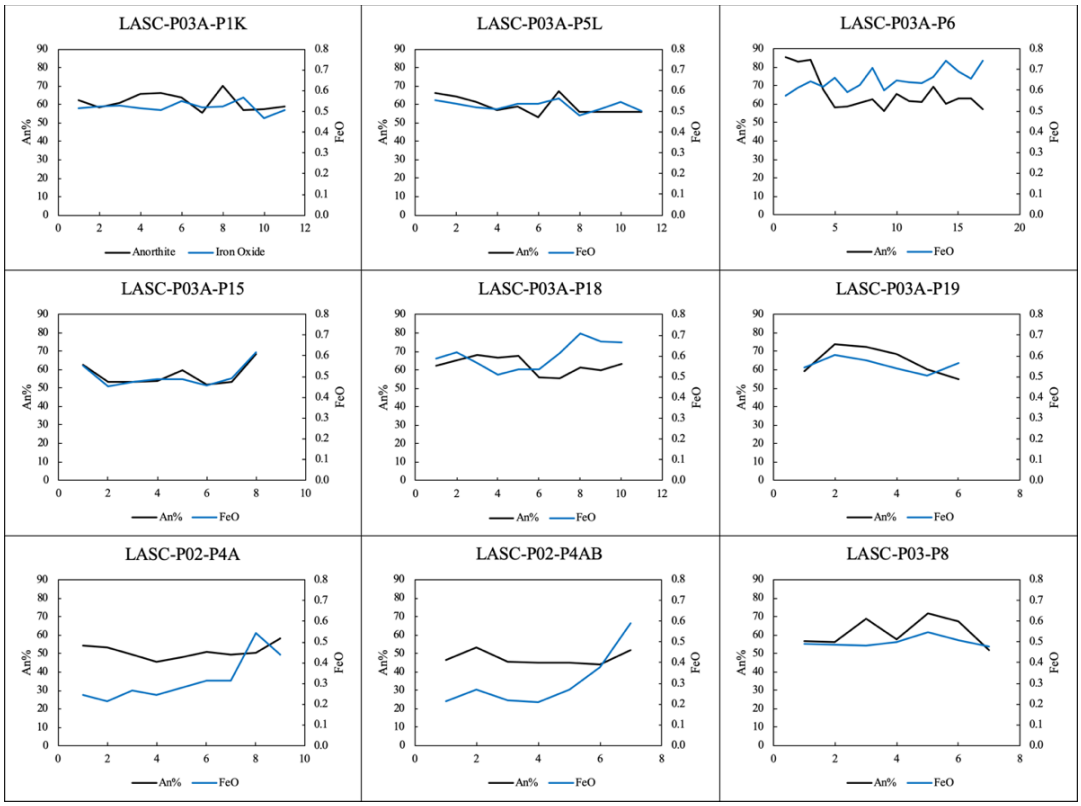

Figure 4. Graphs of plagioclase anorthite content versus FeO wt% for plagioclase from three samples. LASC-P02 is from the Tumbres eruption, LASC-P03 is a felsic portion of the 1993 pumice, and LASC-P03A is the banded 1993 pumice. Change in molar anorthite is represented by the solid black line and change in FeO is represented by the solid blue line. Spikes represent compositional zones of the crystal.

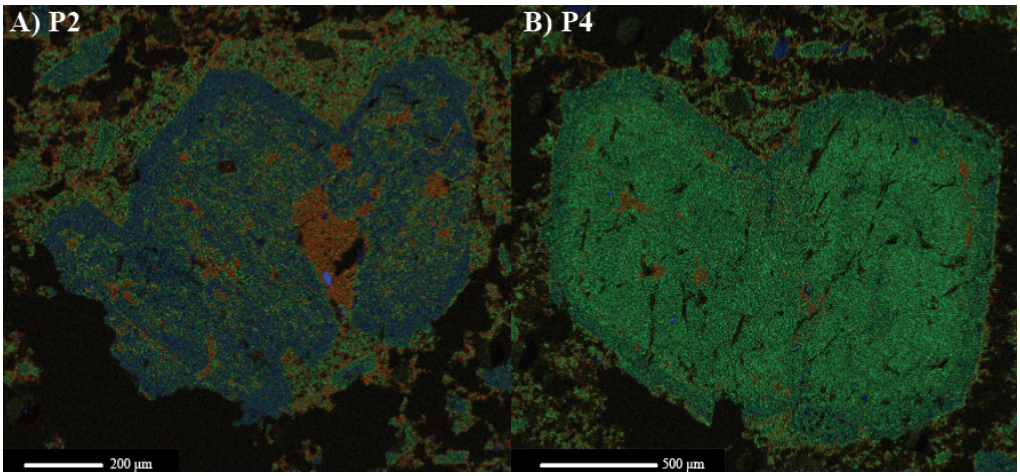

Figure 5. Plagioclase K-Na-Ca chemical maps of A) LASC P02-P2 and B) LASC P02-P5. K is red, Na is green, and Ca is blue. A is more Ca-rich near the rim, shown by the brighter blue color, versus where it is resorbed, it is more Na-rich where it is green, and K-rich where it is orange. B is very strongly Na-rich, though there is more Ca near the rim shown in a slight blue-green. All sample chemical maps can be found in Appendix B.

subhedral to euhedral and display Carlsbad and polysynthetic twinning, with a bladed to tabular shape. Pyroxenes are pale yellow-green in PPL and show excellent cleavage, twinning, and crystal habit with a wide range of sizes. Sparse, anhedral brown hornblende grains possess opacitic rims and are small on average. Fe-Ti oxides are common, and in some cases are >200μm in size. There are glomerocrysts which often contain clinopyroxene, along with the other minerals, and sometimes form around an air pocket. Xenoliths are also present. Some hornblende exhibit alteration textures. All crystals display some level of resorption, often in the form of coarse-grained sieving, and are cracked from eruption.

Table 2. Molar Anorthite, textural description, and population classification of plagioclase.

Sample	An	Textural Description	Type
P02-P1	79.6-77.9	Spongey sieved unzoned high An	High
P02-P2	74.5	Spongey sieved unzoned high An	High
P02-P5A	45.5-58.4	Na-rich, sieved, resorbed outer rim, unzoned low An	Low
P02-P8	51.5-77	Patchy zoning, resorbed outer rim, normal zoned	Normal
P03-P2	49.5-69.4	Oscillatory reverse, resorb rim, Na-rich	Osc
P03-P4	50.7-72.1	Bladed, Na-rich, Ca rim, Spongey sieved	Osc
P03-P7	45.9-61.2	Polygonal, unzoned low to high	Low
P03A-P5	53.6-65.0	Polygonal, Ca core, Na rim	Medium
P03A-P6	85.4-56.1	Resorb rim, fluid inclusions, High Ca	Osc
P03A-P11	48.1-67.9	Spongey, resorb rim, Na core Ca rim	Osc
P03A-P19	54.9-73.7	Patchy core, normal zoned rim, resorbed rim	Normal
P03B-P4	56.5-69.2	Polygonal, resorbed interiors, normal zoned	Normal

The Tumbres samples are a two-pyroxene system with pyroxenes of augite and enstatite. Some pyroxenes have defined oscillatory zoning or near rims of fine-grained sieving and resorption surfaces. Geothermobarometry of clinopyroxene temperatures averaged 1087°C and

pressures averaged 2.4 kbars, or 8.5 km depth (Fig. 3). Orthopyroxene temperatures ranged from 1083 to 1100°C and average pressure is 1.4 kbars, or 5.3 km depth.

Stage IV: April 1993

Stage IV samples are banded pumices erupted in April, 1993. They are represented by three samples denoting the felsic endmember, the mafic endmember, and the banded intermediate section. The samples are vesicular vitrophyric pumices that range from a deep black color for the mafic portion to a buff color for the felsic portion, with the banded sections having layers of both.

The felsic pumices (LASC P03) contain phenocrysts of plagioclase, two-pyroxenes, and a groundmass of Fe-Ti oxides, glass, and vesicles. Plagioclase is the most abundant and largest phenocryst phase. Crystals are subhedral to euhedral, displaying multiple large-grain sieving textures – spongey cores, outer rings of fine-grained sieving, fine-scale oscillatory zoning on rims in addition to melt inclusions and twinning. Pyroxenes are smaller in size on average, ranging from 50-100μm and showing textures more common to medium grained crystals, such as fine-scale oscillatory zoning throughout the crystal and fine-grained sieving in the cores of crystals. All phenocrysts are cracked or fragmented. Glomerocrysts are sparse, but when present, are large and cohesive, with bladed plagioclase and clinopyroxenes. Fe-Ti oxides are also sparse, occasionally displaying euhedral crystal shape. Glass is brown in color and is clustered around larger vesicles.

Molar anorthite ranges from 45.7 to 77.9% and plagioclase phenocryst populations are of primarily unzoned low An oscillatory, and normal zoned types (Table 2). FeO wt% ranges from 0.25 to 0.64, and MgO wt% from 0.026 to 0.086. FeO averages 0.48, and MgO averages 0.047

(Fig. 2). P03 plots generally in the middle of the samples, and FeO has a positive trend and MgO has a negative trend. There are some outliers plotting with low %An and FeO content. The transect from core to rim has consistent FeO wt% values close to 0.5%, and %An ranges between ~50 to 71%, with a constant value at the core then two spikes, one near the core, then a lowered value, than another spike closer to the rim (Fig. 4). %An decreases after this spike towards the rim. Chemical maps show primarily Na-rich crystals, with Ca-rich crystals much less abundant; phenocrysts are dominantly albite-rich in composition, whereas microlites are often more Ca-rich, often in the cores (Fig. 6). However, all crystals have oscillatory Na to Ca zoning, with a zone of high-Ca growth close to the rim, with more Na growth at the rim. This Ca zone is thicker and stronger in some samples (P03-P4) as opposed to others. Some also have multiple oscillations (P03-P2). Resorbed areas in the cores of the crystals have areas of K-rich and Ca-rich melts.

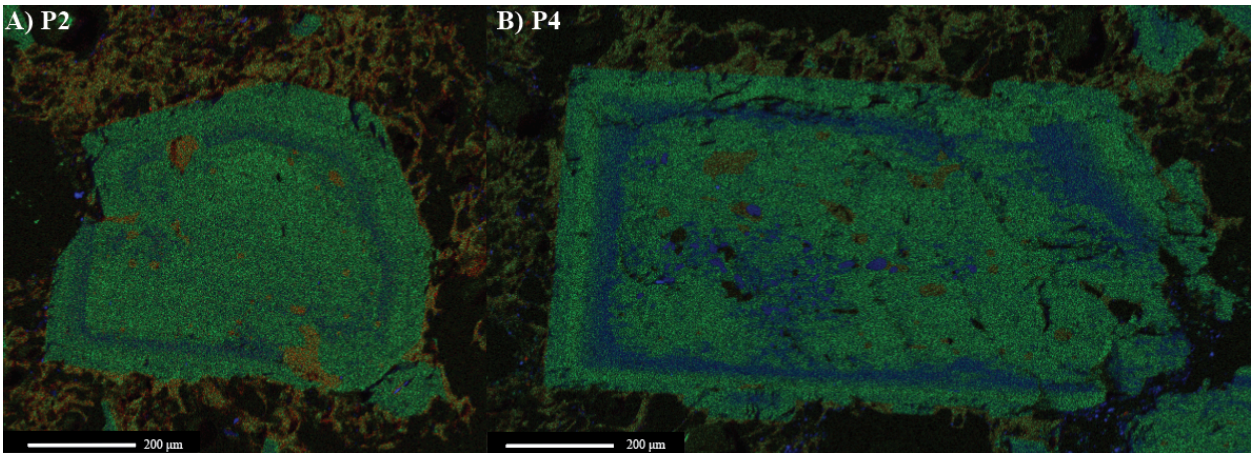

Figure 6. Plagioclase K-Na-Ca chemical maps of A) LASC P03-P2 and B) LASC P03-P4. K is red, Na is green, and Ca is blue. A) shows high Na content with the bright green core, but near the rim there is a Ca-rich zone. B) has a Na-rich core, but has areas of resorption that are very Ca-rich (bright blue) as is the blue zone near the rim. The outside of B is very bright green, showing an increased Na content there.

Mafic samples contain phenocrysts of plagioclase, two-pyroxenes, and groundmass consisting of Fe-Ti oxides, glass, and vesicles. Pyroxenes are more abundant than plagioclase though all crystals are anhedral to subhedral. Crystals lack distinct zonation and are heavily cracked. Clinopyroxene phenocrysts are larger and more abundant than orthopyroxenes and show strong twinning, ranging from 500μm-3mm. Orthopyroxene is more common at microlite size of 100-300μm, and is more rounded than clinopyroxene. Both are commonly in glomerocrysts, which are abundant in the sample and include plagioclase, clinopyroxene, and orthopyroxene. Glass is red-brown to black in color, and vesicles are small to medium in size and irregularly shaped.

Molar anorthite ranges from 56.5 to 80.8% and plagioclase populations are types unzoned low An and normal zoned (Table 3). FeO wt% ranges from 0.505 to 0.716, and MgO ranges from 0.063 to 0.077 (Fig. 2). FeO averages 0.601, and MgO averages 0.071. P03B is on the higher side of all values, but results are hard to determine based on lack of data, and uncertainty is large. This sample has a lower abundance of plagioclase overall, and individual transects and element maps were not collected. The thin section map shows populations of Na- and Ca-rich crystals, though many are cracked and broken, preventing further chemical analysis.

Banded samples contain phenocrysts of plagioclase, two-pyroxenes, and groundmass consisting of Fe-Ti oxides, glass, and vesicles. Mineral abundance differs between light and dark bands, with dark bands having a higher proportion of pyroxenes and light bands having a higher proportion of plagioclase. Clinopyroxenes are the most common pyroxene in the sample, and also the largest in size, ranging from 200μm-2mm. The clinopyroxene phenocrysts in the dark bands are subhedral to euhedral and display twinning. Orthopyroxenes are smaller and round in shape, from 100-500μm. The light bands have lower quality, quantity, and sizes of crystal, with

only some phenocrysts of plagioclase 200μm on average and small anhedral plagioclase microlites <100μm in size mostly incorporated into groundmass. Lighter glass is pale tan to colorless in PPL, and dark glass is brown to black. Between light and dark bands there is mixing textures in the glass. Groundmass is composed of glass, two-pyroxenes, plagioclase, vesicles, and Fe-Ti oxides. All crystals show some form of sieving, whether large grains showing coarse-grained sieving or small grains showing fine-grained sieving. Resorption surfaces are common on small poorly-formed plagioclase crystals in the white bands.

Molar anorthite ranges from 44.7 to 85.6% and all plagioclase populations and textures are represented (Table 3). FeO wt% ranges from 0.35 to 0.74, and MgO wt% from 0.034 to 0.091 (Fig. 2). FeO averages 0.55, and MgO averages 0.06. P03A plots with slightly higher FeO and MgO values than P03, and the high %An are possibly outliers. FeO overall has a positive trend but MgO is too clustered to see any obvious trends. P03A transects stay within a narrow range (Fig. 4). P03A samples on average have FeO content around 0.5%, between 0.4 and 0.6. The two transect outliers are P03A-P6 and P03A-P18, both of which trend around 0.7, especially towards the rim. P6 also fluctuates more than the other samples, which could be due to inclusions or cracks in the crystal. Molar %An for P3A samples ranges around 50-60%. P6 also deviates, but in this case in the core as opposed to the rim. Chemical maps show plagioclase that varies based on the band that it is in (Fig. 7).

Plagioclase in light bands is more Na-rich and have Na cores (P03A-P11), versus the plagioclase from the darker bands that are more Ca-rich and have Ca cores (P03A-P6, P19). All samples show some level of zoning, though in some cases it is more prevalent than others (P6). Resorption in the core of crystals is often K-rich, though this is more abundant in the Ca-rich crystals. All crystals show some level of remelting and vary in shape from polygonal to blade-

like. There are both phenocrysts and microlites, both of which follow similar compositional trends based on the band they are in.

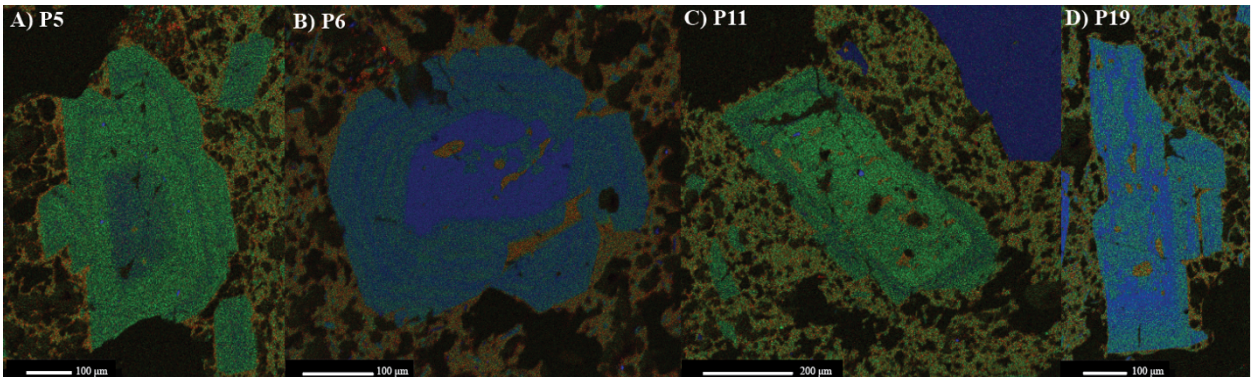

Figure 7. Plagioclase K-Na-Ca chemical maps of A) LASC P03A-P5 B) LASC P03A-P6, C) LASC P03A-P11, D) LASC P03A-P19. P6 and P19 are much more Ca rich and are from the mafic bands of the banded pumice, versus P11 which is from the light band. Notice the scale – this crystal is half the size of the others with strong coarse-grained sieving and resorption surface. P5 has a Ca rich core which becomes Na rich towards the rim. P5 and P6 are both excellent examples of fine-scale oscillation. The deep blues in the cores of B and D are very Ca-rich, and they become lighter and greener as Na content rises.

Plagioclase Geothermometry

Plagioclase analysis was used to find crystallization temperatures of phenocrysts in the Tumbres and 1993 pumices (Fig. 8). All samples have a bimodal distribution of a hotter crystallization and cooler crystallization temperatures. Crystallization temperatures from the April 1993 eruption are on average hotter than the Tumbres eruption.

Whole Rock Geochemistry

Whole rock and pumice major and trace element compositions of Lascar samples are reported in Table 3. Whole-rock samples are pumices are relatively uniform medium-K, calc-alkaline andesites (Fig. 9), which is typical of Central Volcanic Zone stratovolcanoes on the arcfront (Mamani et al., 2010; Michelfelder et al., 2013). SiO_2 ranges from 58.9-62.1 wt%. FeO,

MgO and CaO contents generally decrease with increasing SiO_2, while K_2O, Na_2O and Al_2O_3 contents generally increase (Table 3). TiO_2, P_2O_5 and MnO contents are either uniform or show no relationship to SiO_2 contents.

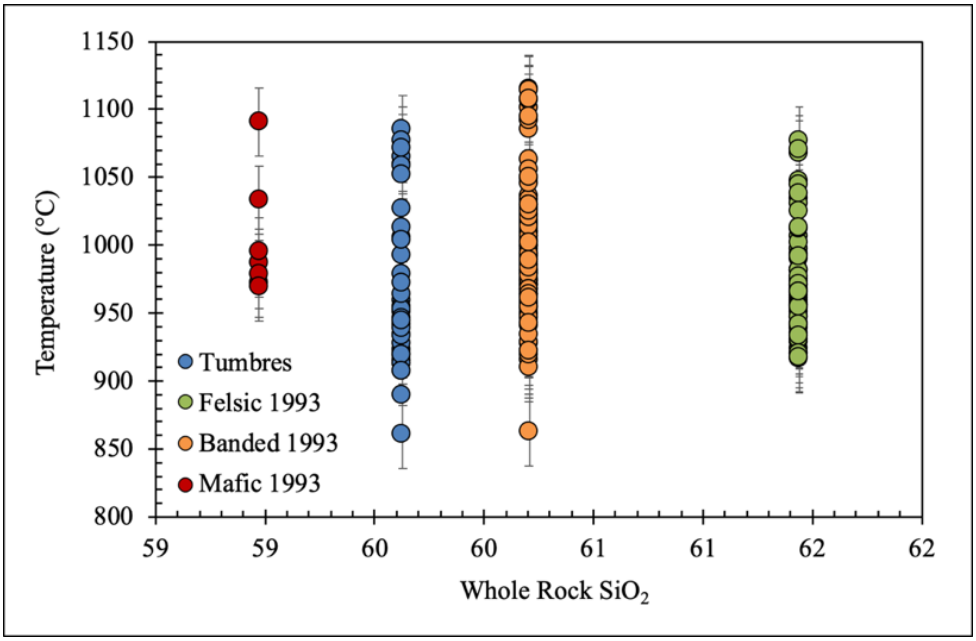

Figure 8. Plagioclase temperature data versus whole rock SiO_2 from pumices. All samples have a higher temperature cluster and a lower temperature cluster, most likely due to changes in core to rim compositions.

Table 3. Whole rock major element data for all samples, separated by stage of activity.

	Stage I				Stage II	Stage III		Stage IV	
Sample	24-01	24-04	24-100	100	P01	25-T01	P02	P03	P03B
SiO^2	61.2	60.3	61	61.5	59.4	58.5	59	61	58.6
TiO^2	0.72	0.73	0.72	0.71	0.77	0.85	0.8	0.72	0.76
Al^2O^3	17.7	17.9	17.7	17.5	16.6	17.3	16.8	16.7	16.5
FeO*	5.27	5.32	5.29	5.09	5.77	6.42	6.26	5.7	6.49
MnO	0.10	0.10	0.10	0.10	0.10	0.11	0.12	0.11	0.12
MgO	2.33	2.39	2.36	2.26	3.72	3.43	3.81	3.43	4.8
CaO	5.74	5.79	5.73	5.74	6.09	7.09	6.73	6.02	7.08
Na^2O	3.97	3.86	3.97	3.94	3.37	3.78	3.39	3.37	3.23
K^2O	1.97	1.94	1.94	1.97	1.83	1.58	1.79	2.04	1.61
P^2O^5	0.24	0.23	0.23	0.23	0.21	0.31	0.25	0.19	0.18

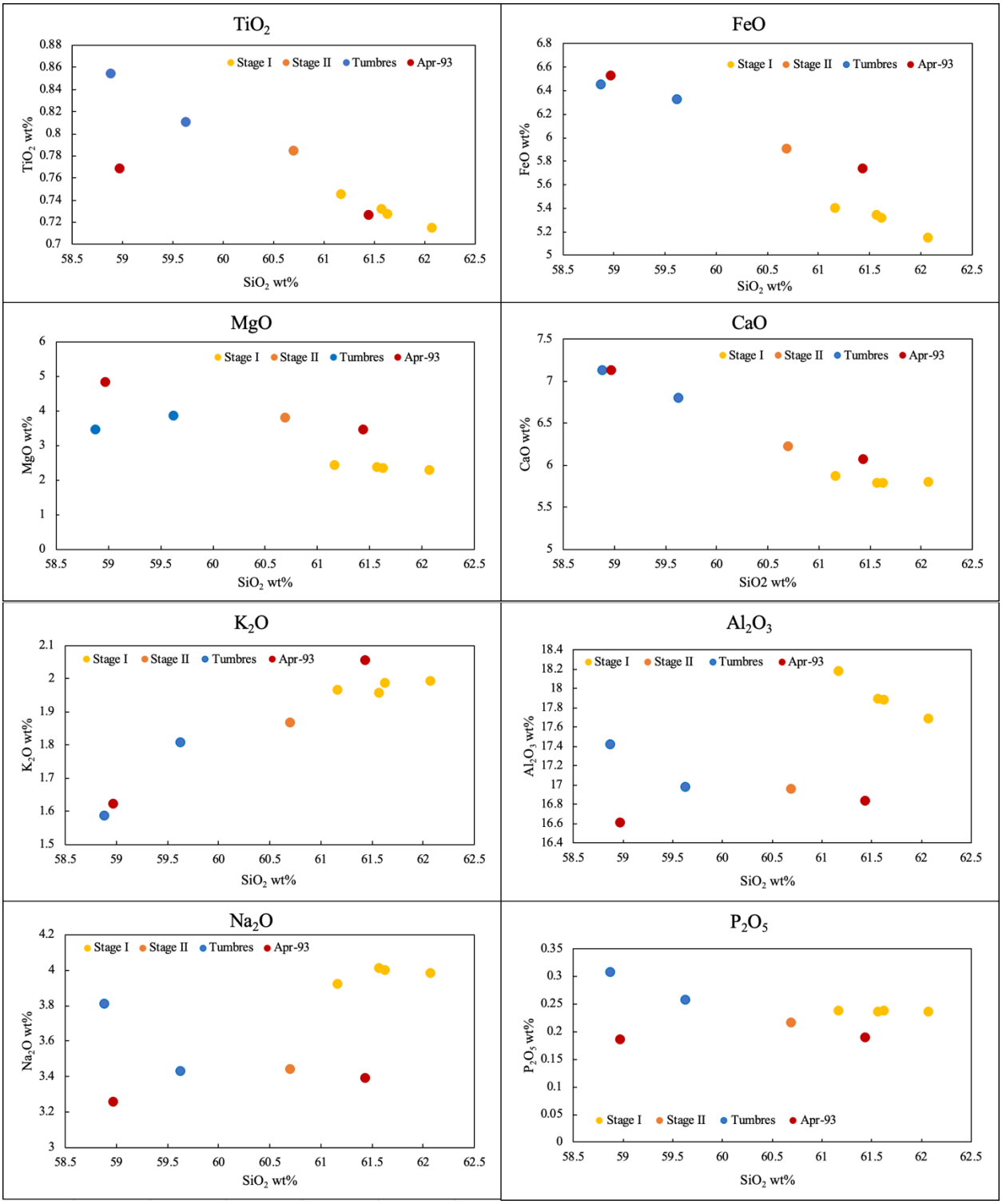

Figure 9. Whole rock element versus SiO_2 wt%. Mafic metals (TiO_2, FeO, MgO, CaO) decrease with continued stages, whereas felsic elements (K_2O, Al_2O_3, Na_2O, P_2O_5) decrease or show no pattern with continued evolution of the chamber.

DISCUSSION

Data collected from plagioclase and pyroxenes provides insight into the conditions of Lascar's magma chamber over time, including changing composition and depth. Pyroxene geothermobarometry provides a range of pressures and temperatures of crystallization that have been interpreted to be a basic model of Lascar's bimodal magma chamber for Stage I and Stage III conditions. Plagioclase data provides ranges of eruption temperatures for the Tumbres and April 1993 eruptions, in addition to chemical maps and petrography, which further constrain the hypothesis of a bimodal magma chamber.

Interpretation of Plagioclase Zoning Patterns

Plagioclase crystals are widely used due to the abundance of information they provide on magma evolution, including water content, temperature, and pressure (Housh and Luhr, 1991; Nelson and Montana, 1992; Putirka, 2005; Streck and Grunder, 2008; Ustunisik et al., 2014; Waters and Lange, 2015; Pizarro et al., 2019). This study used petrologic analysis of plagioclase to infer conditions in the magma chamber during evolution. Anorthite content core to rim zoning and microtextures are especially useful in understanding the processes in the development of the system. Zoning here is defined as changes in chemical abundance from the core to the rim of plagioclase crystals. Crystals in these samples were often complex, with combinations of multiple patterns and textures. The main zoning patterns are normal zoning, reverse zoning, oscillatory zoning, and patchy zoning. Microcrystalline textures are caused by crystallization and dissolution as the conditions of the magma chamber evolve (Streck 2009).

Dissolution textures occur when conditions in the system change and are no longer favorable to the continued crystallization of minerals, at which point they begin to resorb into the

melt. Depending on the cause of the change, different textures can result. Resorption can begin at the rim of the crystal, creating a rounded appearance as opposed to euhedral habit (Fig. 10). This can be due to any number of condition changes. Pervasive resorption in the form of various degrees of sieving are more telling. Fine-sieving occurs in the cores of small crystals, or on the rims of medium to large crystals (Renjith 2014; Fig. 11). It occurs when the parent melt mixes with a Ca-rich melt, causing partial dissolution due to composition changes (Renjith 2014).

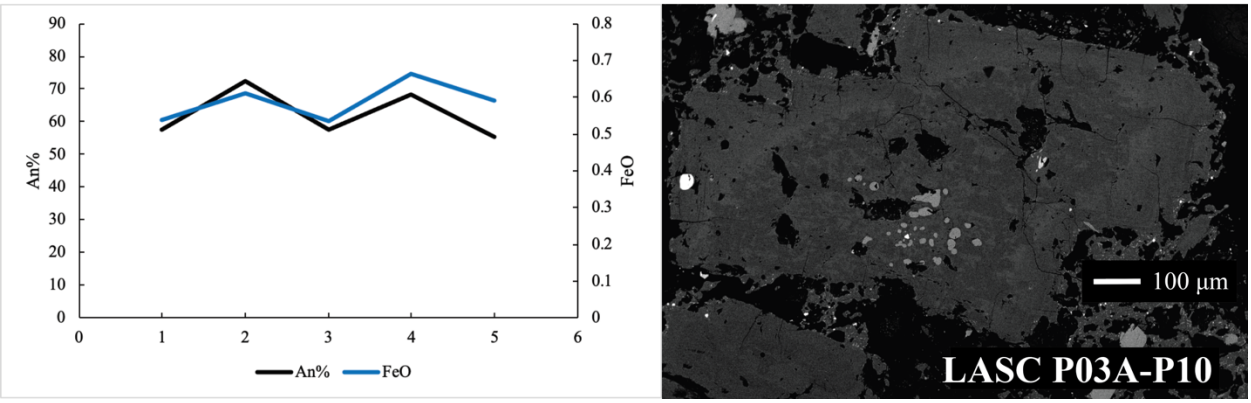

Figure 10. Banded 1993 crystal showing complex growth and dissolution textures. The rounded edges on the right side display dissolution into the melt. The core of the crystal has fine sieving and a likely inherited core, with the growth beyond it normally zoned. Light areas in the core are liquid inclusions. The larger black areas are cellular structure. Transect has saw-toothed pattern with jumps in composition from core to rim.

Spongey textures are different from fine sieving, with larger areas of resorption. It is caused from adiabatic decompression creating a pressure change, remobilizing the structure of the crystal. It occurs not because of compositional changes, but because of pressure changes. Cellular or "boxy" textures are due to rapid growth and quenching and are larger open pockets of resorbed glass (Fig. 10). They are indicative of a sudden change in the temperature of the melt.

Growth textures such as zoning result from the plagioclase crystallizing during cooling. Normal zoning patterns here are defined as decreasing anorthite (An) content towards the rim of a crystal (Streck, 2008; Fig. 10). This pattern is a reflection of the fractionation of the liquid as it

evolves, with anorthite crystallizing out of the melt and changing the composition. Generally, this pattern is indicative of a closed system that has constant water content and pressure. In these crystals, normal zoning typically occurs in the rim of the crystal, outside of a resorbed and often cellular or spongey core.

Reverse zoning patters here are defined as increasing anorthite (An) content towards the rim of a crystal. This pattern is often indicative of an open system with magma mixing with a Ca-rich melt (Streck, 2008). If the crystal was fractionating in a closed chamber, An content would steadily decrease as the magma evolved. If An content increases, this suggests that there is a new source of material that is enriching the melt. This is especially in the case of reverse zoning with increasing Fe content, as that supports new material being added, and not solely increase in temperature. Samples that show reverse zoning in this study nearly all have increasing Fe content with decreasing anorthite content.

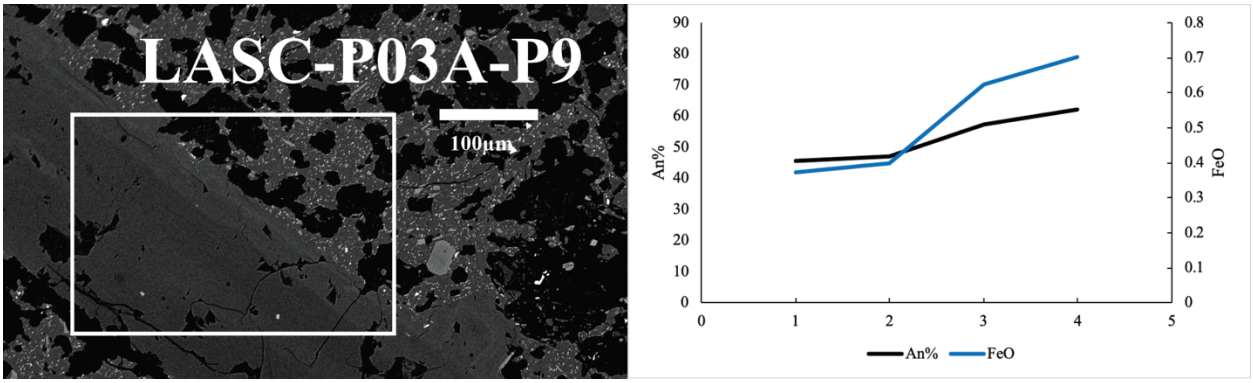

Figure 11. Banded 1993 crystal displaying reverse zoning. The dark, low anorthite core increases in content towards the rim. Transect has rising An% and FeO with magma enrichment.

Patchy zoning is any irregularly distributed zoning pattern in which there are no clear growth zones (Fig. 12). In these samples patchy zonation is often associated with spongey and cellular structures. Patchy zoning in this study is commonly in the core of the crystal, often with

a different pattern of zoning on the rim. This is thought to be caused by the core being inherited from a previous magma – a crystal from a previous eruption that is forced out of equilibrium by an injection of melt, which causes it to dissolve. Once the crystal re-equilibrates, crystal fractionation can resume. This complex case is most commonly found in the felsic 1993 pumices, with a spongey or patchy core with a reverse or normally zoned rim. This is evidence for a magmatic rejuvenation changing the composition of the melt during the evolution of these crystals.

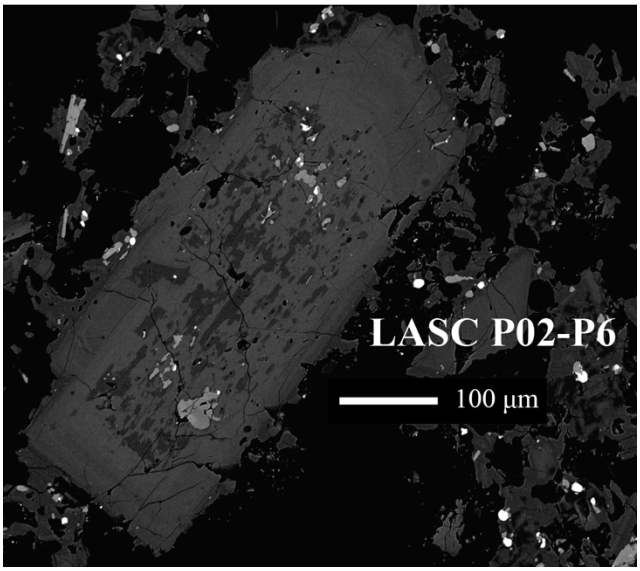

Figure 12. Tumbres plagioclase displaying patchy zoning. Low anorthite patchy zoning in the core with a high anorthite normally zoned rim that switches to oscillatory zoning. There are dissolution surfaces on the edge of the patchy core and on the outer rim.

Oscillatory zoning is also prevalent in these plagioclase crystals, here defined as rings of composition changes that reflect changing melt composition (Fig. 13). This type of zoning can be formed via kinetic effects by magma mixing or by large-scale changes in the system depending on oscillation size (Ginibre et al., 2007). Fine-scale zoning represent small-scale variations at the crystal-melt interface, which also supports a model of changing reservoir conditions on a more localized scale (Renjith, 2014). Thin bands are a sign of high-frequency growth and dissolution

in the crystal as the small changes switch the process the crystal is undergoing. Oscillations that show dissolution surfaces are likely caused by magma rejuvenation and change in magma chamber chemistry, causing the crystal to begin diffusing for a longer period of time before recrystallizing again (Ginibre et al., 2007). Oscillatory zoning is one of the most common forms of plagioclase growth and is found in every sample in this study (Fig. 13).

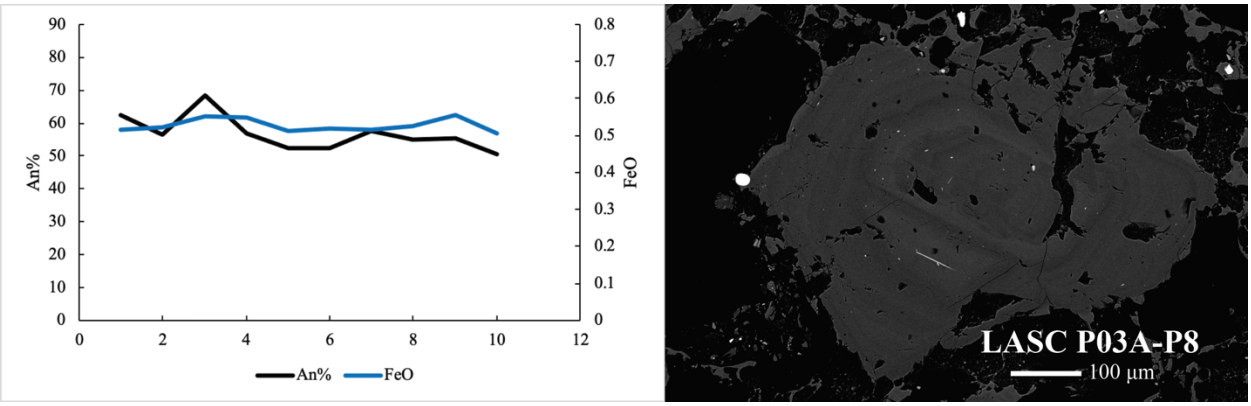

Figure 13. Banded 1993 crystals displaying oscillatory zoning. The large stepwise rings suggest compositional magma mixing, whereas the fine-scale outer rings are more likely formed by kinetic processes.

Lascar Plagioclase

Plagioclase from the Tumbres pumice often have patchy sieving, with areas of low An content in the core surrounded by rims with high An content (Fig. 10). These suggest that these crystals were either in the process of re-equilibration via diffusion or that there was crystal growth around a skeletal structure (Streck, 2008). Rims of crystals are also usually resorbed in shape or are in the processes of resorbing. Some crystals have sodic cores and mostly sodic rims, whereas others are very strongly calcic and only possess sodic dissolution surfaces. This shows that there are crystals from two different parent melts – a mafic, and a silicic.

Plagioclase from the 1993 eruption have textures and compositions that are specific to their composition and are different than the Tumbres pumice. The felsic products had almost

exclusively sodic cores and rims, but almost all had one near-rim band of very-high Ca-rich composition. This suggests that crystals experienced an influx of a magma of a mafic composition at some point in their crystallization history, but that it was not exposed to it for very long before returning to a Na-rich melt. The mafic composition pumice did not contain plagioclase that was of high enough quality to analyze, or really very much plagioclase at all – there was most likely not time during its development to crystallize the phenocrysts that the other pumices contained. The intermediate banded pumice has a wide variety of crystal compositions and textures. A higher proportion of plagioclase phenocrysts have Na-rich cores as opposed to Ca-rich cores, though many have Ca-rich bands near their rim.

Anorthite content in the banded samples varies greatly from crystal to crystal, many showing patchy zoning or resorbed boxy-cellular structures. These crystals often have outer rims that are normally zoned, fine-scale oscillatory zoning, or are monotonous. This might be due to the core of the crystal being a xenocryst assimilated from the country rock, or an antecryst left in the chamber after the Tumbres eruption.

Other crystals have much more consistent compositions with oscillations that are close together in composition, or relatively smooth reverse zoning patterns. Many crystals are highly dissolved both in cores and rims, and often have fluid inclusions. This suggests that the plagioclase in this sample underwent a variety of processes, and not all of them had the same evolutionary path. There are broken textures but also synneusis, which suggests strong convection at the crystal-melt boundary (Renjith, 2014). A wide variety of compositions, zoning patterns, and textures all support the hypothesis that magma mixing was occurring in this system between a sodic and a calcic melt.

Recharge and Storage History at Lascar

Decreases in core-to-rim anorthite content, strong dissolution and regrowth textures, and nearly bimodal compositions of Ca-rich and Na-rich plagioclase crystals all suggest that the crystals in the Lascar volcano magma chamber grew in a system that is characterized by periodic recharge events of a more mafic, Ca-rich magma into Na-rich magma. Pyroxene and plagioclase temperatures show crystals forming in varying conditions, with plagioclase crystallizing at a lower temperature than the pyroxenes. Pyroxenes are also well-formed and abundant in the mafic products in multiple stages of Lascar's eruptive history. This suggests that pyroxenes were crystallizing not only at greater temperatures than the plagioclase, but also at greater depths, possibly from a magma of different composition that was injected into the magma chamber. Whole rock trends show decreasing silica and felsic elements and increasing mafic elements with continued evolution of the chamber, also suggesting periodic influxes of mafic material changing the composition of the system over time (Fig. 9).

While there is ample evidence for the bimodal nature of Lascar's chamber and the existence of recharge events in its history, the source of the silicic magma in the system cannot be accurately determined at this time. Whole rock compositions between rocks from APMB-sourced eruptions elsewhere in the APVC do not correlate strongly with the samples analyzed at Lascar. The earliest, most felsic samples from Lascar's Stage I dome-building eruptions are not as silicic or compositionally similar to other volcanoes in the APVC, with much higher metal content and lower calc-alkaline content (Michelfelder et al., 2013). Plagioclase crystals have varying core compositions, even within the Na-rich groupings. The APMB is very large and homogeneous, and if the crystals were sourced from that magma, the core compositions would be similar to one another, which they are not. The source of the magma could be better

constrained by $^{87}Sr/^{86}Sr$ analysis, as this signature is specific for the APMB and would give strong evidence for the relationship, or lack thereof, between Lascar and the APMB. Depths of crystallization for Lascar's crystals tend to be around 3 to 5 km depth, which is barely the top of the APMB, whose main body is between 10 to 15 km deep (Pritchard et al., 2018).

A more likely model for the system feeding Lascar volcano is one sourced by multiple smaller reservoirs producing melts of differing compositions that mix together in a shallow chamber (Fig. 14). This explains the varying compositions throughout Lascar's eruptive periods and within single eruptions, and the difference in composition between the core and rim of crystals. Support of this is the discrete crystallization ages for clinopyroxenes in Stage I block and ash flows (Fig. 3). There is a population between the surface and 6 km deep and another around 21 km. This pronounced gap could be the difference between a deep source magma and the depth of Lascar's reservoir. Another example of this is the hotter crystallization temperatures for plagioclase (Fig. 8). This could be due to differences in temperature between the core and rim conditions of the crystals. If these crystals had begun crystallizing in the APMB, the majority of their depths would be between 10 to 15 km depth, and depths would be in a general range around those temperatures, without significant gaps. There is no evidence of any correlation at this point, but further research would be necessary to definitely prove relation either way.

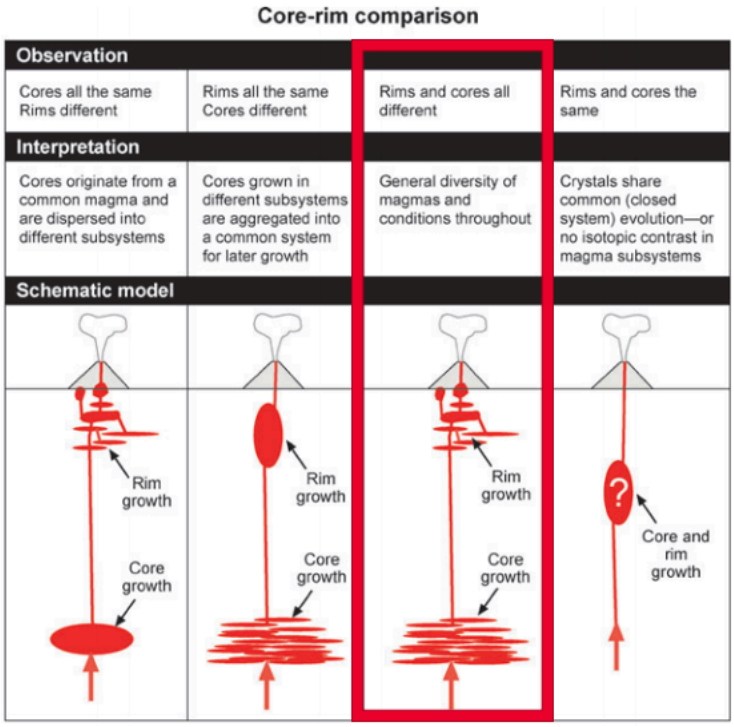

Figure 14. Model of magma chamber from Davidson et al., 2007. Differences between core and rim growth in all samples suggest a model with multiple smaller magma chambers at both a shallow level and at depth.

CONCLUSIONS

Lascar volcano is a complex system that seems to be influenced by multiple smaller isolated magma chambers, with no clear connection to the APMB. The average depths of crystallization for the majority of Lascar's crystals averages around 6 km depth, but populations vary depending on crystal type and eruption. Plagioclase and pyroxene mineral chemistry, texture and petrography provide insight into the evolution of this magma chamber, allowing us to create a more accurate model of this system. The range of data collected suggests that Lascar is not fed from a single large reservoir, but a series of smaller reservoirs with varying mineral chemistries, temperatures, and depths. This explains the unique composition of each eruption in Lascar's history. These new data support the ongoing hypothesis that Lascar volcano has a bimodal magma chamber; however, the hypothesis that magma injection triggers volcanic events cannot be proved by the data collected at this time. Further research into the specific timescales of crystallization, coupled with the temperature and pressure data acquired in this study, could shed light on the evolution of this volcano, and therefore many other volcanoes in the CVZ.

REFERENCES

Allmendinger, R.W., Jordan, T.E., Kay, S.M., and Isacks, B.L., 1997, the Evolution of the Altiplano-Puna Plateau of the Central Andes: Annual Review of Earth and Planetary Sciences, v. 25, p. 139–174, doi:10.1146/annurev.earth.25.1.139.

Annen, C., 2009, From plutons to magma chambers: Thermal constraints on the accumulation of eruptible silicic magma in the upper crust: Earth and Planetary Science Letters, v. 284, p. 409–416, doi:10.1016/j.epsl.2009.05.006.

Bachmann, O., and Huber, C., 2016, Silicic magma reservoirs in the Earth's crust: American Mineralogist, v. 101, p. 2377–2404, doi:10.2138/am-2016-5675.

Beck, S.L., Zandt, G., Ward, K.M., Scire, A., Beck, S.L., and Ward, K.M., 2015, Multiple styles and scales of lithospheric foundering beneath the Puna Plateau, central Andes: GSA memoir 212, v. 1212, p. 43–60, doi:10.1130/2015.1212(03).

Bégué, F., Deering, C.D., Gravley, D.M., Kennedy, B.M., Chambefort, I., Gualda, G.A.R., and Bachmann, O., 2014, Extraction, storage and eruption of multiple isolated magma batches in the paired Mamaku and Ohakuri eruption,Taupo volcanic zone, New Zealand: Journal of Petrology, v. 55, p. 1653–1684, doi:10.1093/petrology/egu038.

Bergantz, G.W., Schleicher, J.M., and Burgisser, A., 2015, Open-system dynamics and mixing in magma mushes: Nature Geoscience, v. 8, p. 793–796, doi:10.1038/ngeo2534.

Burns, D.H., de Silva, S.L., Tepley, F., Schmitt, A.K., and Loewen, M.W., 2015, Recording the transition from flare-up to steady-state arc magmatism at the Purico-Chascon volcanic complex, northern Chile: Earth and Planetary Science Letters, v. 422, p. 75–86, doi:10.1016/j.epsl.2015.04.002.

Caracciolo, A., Bali, E., Guðfinnsson, G.H., Kahl, M., Halldórsson, S.A., Hartley, M.E., and Gunnarsson, H., 2020, Temporal evolution of magma and crystal mush storage conditions in the Bárðarbunga-Veiðivötn volcanic system, Iceland: Lithos, v. 352–353, doi:10.1016/j.lithos.2019.105234.

Coira, B., Davidson, J., Mpodozis, C., and Ramos, V., 1982, Tectonic and magmatic evolution of the Andes of northern Argentina and Chile: Earth Science Reviews, v. 18, p. 303–332,

doi:10.1016/0012-8252(82)90042-3.

Cooper, K.M., 2017, What does a magma reservoir look like? the “crystal’s-eye” view: Elements, v. 13, p. 23–28, doi:10.2113/gselements.13.1.23.

Cooper, K.M., and Kent, A.J.R., 2014, Rapid remobilization of magmatic crystals kept in cold storage: Nature, v. 506, p. 480–483, doi:10.1038/nature12991.

Davidson, J.P., Morgan, D.J., Charlier, B.L.A., Harlou, R., and Hora, J.M., 2007, Microsampling and Isotopic Analysis of Igneous Rocks: Implications for the Study of Magmatic Systems: Annual Review of Earth and Planetary Sciences, v. 35, p. 273–311, doi:10.1146/annurev.earth.35.031306.140211.

Déruelle, B., Figueroa, O., Medina, E., Viramonte, J.G., and Maragaño, C.., 1996, Petrology of pumices of April 1993 eruption of Lascar (Atacama, Chile): Terra Nova, v. 8, p. 191–199.

Díaz, D., Brasse, H., and Ticona, F., 2012, Conductivity distribution beneath Lascar volcano (Northern Chile) and the Puna, inferred from magnetotelluric data: Journal of Volcanology and Geothermal Research, v. 217–218, p. 21–29, doi:10.1016/j.jvolgeores.2011.12.007.

Díaz, D., Heise, W., and Zamudio, F., 2015, Three-dimensional resistivity image of the magmatic system beneath Lastarria volcano and evidence for magmatic intrusion in the back arc (northern Chile): Geophysical Research Letters, v. 42, p. 5212–5218, doi:10.1002/2015GL064426.

Edmonds, M., Cashman, K. V., Holness, M., and Jackson, M., 2019, Architecture and dynamics of magma reservoirs: Philosophical Transactions of the Royal Society A: Mathematical, Physical and Engineering Sciences, v. 377, doi:10.1098/rsta.2018.0298.

Farrell, A.K., McNutt, S.R., and Thompson, G., 2017, Seismic attenuation, time delays, and raypath bending of teleseisms beneath Uturuncu volcano, Bolivia: Geosphere, v. 13, p. 699–722, doi:10.1130/GES01354.1.

Gardeweg, M.C., Sparks, R.S.J., and Matthews, S.J., 1998, Evolution of Lascar Volcano, Northern Chile: Journal of the Geological Society, v. 155, p. 89–104, doi:10.1144/gsjgs.155.1.0089.

Gelman, S.E., Deering, C.D., Bachmann, O., Huber, C., and Gutiérrez, F.J., 2014, Identifying the crystal graveyards remaining after large silicic eruptions: Earth and Planetary Science Letters, v. 403, p. 299–306, doi:10.1016/j.epsl.2014.07.005.

Ginibre, C., and Davidson, J.P., 2014, Sr isotope zoning in plagioclase from parinacota volcano (Northern Chile): Quantifying magma mixing and crustal contamination: Journal of Petrology, v. 55, p. 1203–1238, doi:10.1093/petrology/egu023.

Ginibre, C., Wörner, G., and Kronz, A., 2007, Crystal zoning as an archive for magma evolution: Elements, v. 3, p. 261–266, doi:10.2113/gselements.3.4.261.

González, C., Inostroza, M., Aguilera, F., González, R., Viramonte, J., and Menzies, A., 2015, Heat and mass flux measurements using Landsat images from the 2000-2004 period, Lascar volcano, northern Chile: Journal of Volcanology and Geothermal Research, v. 301, p. 277–292, doi:10.1016/j.jvolgeores.2015.05.009.

Gualda, G.A.R., Gravley, D.M., Connor, M., Hollmann, B., Pamukcu, A.S., Bégué, F., Ghiorso, M.S., and Deering, C.D., 2018, Climbing the crustal ladder: Magma storage-depth evolution during a volcanic flare-up: Science Advances, v. 4, p. 1–10, doi:10.1126/sciadv.aap7567.

Harmon, R.S., Barreiro, B.A., Moorbath, S., Hoefs, J., Francis, P.W., Thorpe, R.S., Deruelle, B., McHugh, J., and Viglino, J.A., 1984, Regional O-, Sr-, and Pb-isotope relationships in late Cenozoic calc-alkaline lavas of the Andean Cordillera: Journal of the Geological Society, v. 141, p. 803–822, doi:10.1144/gsjgs.141.5.0803.

Henderson, S.T., and Pritchard, M.E., 2013, Decadal volcanic deformation in the central andes volcanic zone revealed by InSAR time series: Geochemistry, Geophysics, Geosystems, v. 14, p. 1358–1374, doi:10.1002/ggge.20074.

Housh, T.B., and Luhr, J.F., 1991, Plagioclase-melt equilibria in hydrous systems: American Mineralogist, v. 76, p. 477–492.

Kendrick, E., Bevis, M., Smalley, R., Brooks, B., Vargas, R.B., Lauría, E., and Fortes, L.P.S., 2003, The Nazca-South America Euler vector and its rate of change: Journal of South American Earth Sciences, v. 16, p. 125–131, doi:10.1016/S0895-9811(03)00028-2.

Kern, J.M., de Silva, S.L., Schmitt, A.K., Kaiser, J.F., Iriarte, A.R., and Economos, R., 2016, Geochronological imaging of an episodically constructed subvolcanic batholith: U-Pb in zircon chronochemistry of the Altiplano-Puna Volcanic Complex of the Central Andes: Geosphere, v. 12, p. 1054–1077, doi:10.1130/GES01258.1.

Mamani, M., Tassara, A., and Wörner, G., 2008, Composition and structural control of crustal domains in the central Andes: Geochemistry, Geophysics, Geosystems, v. 9, doi:10.1029/2007GC001925.

Marsh, B.D., 2006, Dynamics of Magmatic systems: Elements, v. 2, p. 287–292, doi:https://doi.org/10.1016/S0074-6142(09)60100-5.

Matthews, S.J., Jones, A.P., and Gardeweg, M.C., 1994, Lascar volcano, northern Chile; evidence for steady-state disequilibrium: Journal of Petrology, v. 35, p. 401–432, doi:10.1093/petrology/35.2.401.

Matthews, S.J., Sparks, R.S.J., and Gardeweg, M.C., 1999, The Piedras Grandes-Soncor eruptions, Lascar Volcano, Chile; evolution of a zoned magma chamber in the Central Andean upper crust: Journal of Petrology, v. 40, p. 1891–1919, doi:10.1093/petroj/40.12.1891.

Michelfelder, G., Feeley, T., Wilder, A., and Klemetti, E., 2013, Modification of the Continental Crust by Subduction Zone Magmatism and Vice-Versa: Across-Strike Geochemical Variations of Silicic Lavas from Individual Eruptive Centers in the Andean Central Volcanic Zone: Geosciences, v. 3, p. 633–667, doi:10.3390/geosciences3040633.

Nelson, S.T., and Montana, A., 1992, Sieve-textured plagioclase in volcanic rocks produced by rapid decompression: American Mineralogist, v. 77, p. 1242–1249.

Oppenheimer, C., Francis, P.W., Rothery, D.A., Carlton, R.W.T., and Glaze, L.S., 1993, Infrared image analysis of volcanic thermal features: Lascar Volcano, Chile, 1984-1992: Journal of Geophysical Research, v. 98, p. 4269–4286, doi:10.1029/92JB02134.

Pavez, A., Remy, D., Bonvalot, S., Diament, M., Gabalda, G., Froger, J.L., Julien, P., Legrand, D., and Moisset, D., 2006, Insight into ground deformations at Lascar volcano (Chile) from SAR interferometry, photogrammetry and GPS data: Implications on volcano dynamics and future space monitoring: Remote Sensing of Environment, v. 100, p. 307–320, doi:10.1016/j.rse.2005.10.013.

Pizarro, C., Parada, M.A., Contreras, C., and Morgado, E., 2019, Cryptic magma recharge associated with the most voluminous 20th century eruptions (1921, 1948 and 1971) at Villarrica Volcano: Journal of Volcanology and Geothermal Research, v. 384, p. 48–63, doi:10.1016/j.jvolgeores.2019.07.001.

Pritchard, M.E. et al., 2018, Synthesis: PLUTONS: Investigating the relationship between pluton growth and volcanism in the Central Andes: Geosphere, v. 14, p. 954–982, doi:10.1130/GES01578.1.

Putirka, K.D., 2005, Igneous thermometers and barometers based on plagioclase + liquid equilibria: Tests of some existing models and new calibrations: American Mineralogist, v. 90, p. 336–346, doi:10.2138/am.2005.1449.

Renjith, M.L., 2014, Micro-textures in plagioclase from 1994-1995 eruption, Barren Island Volcano: Evidence of dynamic magma plumbing system in the Andaman subduction zone: Geoscience Frontiers, v. 5, p. 113–126, doi:10.1016/j.gsf.2013.03.006.

Rogers, G., and Hawkesworth, C.J., 1989, A geochemical traverse across the North Chilean Andes: evidence for crust generation from the mantle wedge: Earth and Planetary Science Letters, v. 91, p. 271–285, doi:10.1016/0012-821X(89)90003-4.

de Silva, S.L., 1989, Geochronology and stratigraphy of the ignimbrites from the 21 30S to 23 30S portion of the Central Andes of northern Chile: Journal of Volcanology and Geothermal Research, v. 37, p. 93–131, doi:10.1016/0377-0273(89)90065-6.

De Silva, S., Zandt, G., Trumbull, R., Viramonte, J.G., Salas, G., and Jiménez, N., 2006, Large ignimbrite eruptions and volcano-tectonic depressions in the Central Andes: a thermomechanical perspective: Geological Society, London, Special Publications, v. 269, p. 47–63, doi:10.1144/GSL.SP.2006.269.01.04.

Streck, M.J., 2008, Mineral textures and zoning as evidence for open system processes: Reviews in Mineralogy and Geochemistry, v. 69, p. 595–622, doi:10.2138/rmg.2008.69.15.

Streck, M.J., and Grunder, A.L., 2008, Phenocryst-poor rhyolites of bimodal, tholeiitic provinces: The Rattlesnake Tuff and implications for mush extraction models: Bulletin of Volcanology, v. 70, p. 385–401, doi:10.1007/s00445-007-0144-3.

Tassi, F., Aguilera, F., Vaselli, O., Medina, E., Tedesco, D., Delgado Huertas, A., Poreda, R., and Kojima, S., 2009, The magmatic- and hydrothermal-dominated fumarolic system at the Active Crater of Lascar volcano, northern Chile: Bulletin of Volcanology, v. 71, p. 171–183, doi:10.1007/s00445-008-0216-z.

Ustunisik, G., Kilinc, A., and Nielsen, R.L., 2014, New insights into the processes controlling compositional zoning in plagioclase: Lithos, v. 200–201, p. 80–93, doi:10.1016/j.lithos.2014.03.021.

Ward, K.M., Delph, J.R., Zandt, G., Beck, S.L., and Ducea, M.N., 2017, Magmatic evolution of a Cordilleran flare-up and its role in the creation of silicic crust: Scientific Reports, v. 7, p. 1–8, doi:10.1038/s41598-017-09015-5.

Waters, L.E., and Lange, R.A., 2015, An updated calibration of the plagioclase-liquid hygrometer-thermometer applicable to basalts through rhyolites: American Mineralogist, v. 100, p. 2172–2184, doi:10.2138/am-2015-5232.

de Zeeuw-van Dalfsen, E., Richter, N., González, G., and Walter, T.R., 2017, Geomorphology and structural development of the nested summit crater of Láscar Volcano studied with Terrestrial Laser Scanner data and analogue modelling: Journal of Volcanology and Geothermal Research, v. 329, p. 1–12, doi:10.1016/j.jvolgeores.2016.09.018.

APPENDICES

Appendix A-1. Plagioclase major element concentrations, end member, and temperature data (Druitt et al., 2012).

	Concentration									End Member			
Sample	SiO_2	TiO_2	Al_2O_3	FeO	MgO	CaO	Na_2O	K_2O	BaO	%An	%Ab	%Or	T °C
LASC-P03-P1	55.9	0.02	29.0	0.44	0.04	10.6	5.00	0.38	0.06	52.8	44.9	2.24	951
LASC-P03-P1a	55.7	0.03	28.9	0.42	0.04	10.7	4.91	0.39	0.02	53.3	44.4	2.30	953
LASC-P03-P7A	55.6	0.02	29.2	0.43	0.05	10.8	4.86	0.39	-0.02	53.8	43.9	2.30	956
LASC-P03-P7B	54.9	0.02	29.6	0.44	0.04	11.1	4.65	0.30	-0.07	55.9	42.3	1.82	966
LASC-P03-P7C	57.9	0.02	27.8	0.42	0.05	9.1	5.60	0.49	-0.02	45.9	51.1	2.94	917
LASC-P03-P7D	57.0	0.00	27.7	0.43	0.05	9.4	5.46	0.47	-0.07	47.3	49.8	2.82	924
LASC-P03-P7E	55.5	0.03	29.2	0.46	0.05	10.8	4.89	0.37	0.06	53.7	44.1	2.18	955
LASC-P03-P7F	53.2	0.03	30.2	0.49	0.04	12.3	4.12	0.27	-0.06	61.2	37.2	1.59	993
LASC-P03-P6A	53.6	0.03	30.5	0.54	0.05	12.1	4.17	0.76	0.04	58.9	36.6	4.42	982
LASC-P03-P6B	49.0	0.03	33.8	0.59	0.03	15.8	2.40	0.11	0.06	77.9	21.4	0.66	1077
LASC-P03-P6C	56.1	0.01	28.7	0.47	0.06	10.4	5.08	0.36	0.10	52.0	45.9	2.12	947
LASC-P03-P6D	49.5	0.00	33.4	0.51	0.04	15.3	2.59	0.12	-0.09	76.0	23.2	0.72	1067

LASC-P03-P6E	54.7	0.08	29.9	0.48	0.05	11.5	4.64	0.31	0.05	56.7	41.5	1.80	970
LASC-P03-P6F	49.6	0.00	33.6	0.51	0.04	15.6	2.54	0.12	-0.02	76.6	22.6	0.71	1070
LASC-P03-P5A	56.9	0.01	28.2	0.36	0.03	9.6	5.38	0.46	-0.10	48.3	49.0	2.75	928
LASC-P03-P5B	56.6	0.02	29.0	0.46	0.05	10.3	5.18	0.43	0.01	51.0	46.5	2.52	942
LASC-P03-P4A	53.3	0.01	30.5	0.54	0.05	12.1	4.20	0.27	0.03	60.5	37.9	1.62	989
LASC-P03-P4B	56.7	0.01	28.6	0.56	0.05	10.1	5.16	0.40	0.02	50.7	47.0	2.37	940
LASC-P03-P4C	51.0	0.07	32.5	0.48	0.03	14.6	3.01	0.14	-0.02	72.1	27.0	0.85	1048
LASC-P03-P4D	55.1	0.03	29.0	0.49	0.05	10.9	4.79	0.37	0.04	54.5	43.3	2.20	959
LASC-P03-P2A	54.0	0.05	30.2	0.52	0.03	11.8	4.37	0.30	0.07	58.9	39.3	1.78	981
LASC-P03-P2B	56.5	0.00	28.0	0.47	0.05	9.8	5.23	0.42	0.06	49.5	47.9	2.53	935
LASC-P03-P2C	55.4	0.02	29.2	0.48	0.05	11.0	4.79	0.35	-0.04	54.8	43.2	2.06	961
LASC-P03-P2D	56.8	0.04	27.3	0.65	0.09	9.7	4.81	0.71	0.13	50.3	45.3	4.40	939
LASC-P03-P2E	51.5	0.04	31.9	0.50	0.04	14.0	3.27	0.18	-0.05	69.4	29.5	1.09	1034
LASC-P03-P2F	53.3	0.00	30.7	0.44	0.05	12.5	4.08	0.26	0.07	62.0	36.5	1.54	997
LASC-P03-P2G	55.1	0.02	30.4	0.51	0.04	12.0	4.43	0.29	0.05	59.0	39.4	1.69	982
LASC-P03-P2H	53.7	0.01	30.5	0.51	0.06	12.3	4.15	0.28	0.05	61.0	37.3	1.63	992

LASC-P03-P2I	54.9	0.03	29.6	0.48	0.05	11.2	4.72	0.33	0.03	55.5	42.5	1.98	965
LASC-P03-P2J	55.0	0.01	29.5	0.49	0.05	11.1	4.75	0.34	0.01	55.1	42.8	2.03	962
LASC-P03-P8A	55.0	0.02	29.7	0.49	0.05	11.4	4.61	0.30	-0.02	56.7	41.6	1.75	970
LASC-P03-P8B	54.8	0.02	29.6	0.49	0.04	11.3	4.68	0.32	0.04	56.1	42.0	1.90	967
LASC-P03-P8C	51.7	0.01	32.2	0.48	0.05	13.7	3.31	0.19	0.10	68.8	30.1	1.13	1031
LASC-P03-P8D	54.7	0.02	29.7	0.50	0.04	11.5	4.47	0.30	-0.07	57.7	40.5	1.79	975
LASC-P03-P8E	50.7	0.01	32.7	0.55	0.04	14.5	3.09	0.15	0.01	71.5	27.6	0.89	1044
LASC-P03-P8F	51.8	0.00	31.5	0.51	0.05	13.6	3.48	0.20	-0.01	67.6	31.2	1.16	1025
LASC-P03-P8G	55.9	0.03	28.6	0.48	0.05	10.4	5.08	0.34	0.06	52.0	46.0	2.02	947
LASC-P03-P9A	56.8	-0.01	27.5	0.44	0.06	9.7	5.34	0.44	0.08	48.7	48.7	2.61	930
LASC-P03-P9B	56.0	0.00	28.5	0.45	0.04	10.3	5.22	0.42	0.05	50.8	46.7	2.45	941
LASC-P03-P10A	57.6	0.05	28.0	0.25	0.04	9.4	5.58	0.50	0.01	46.7	50.3	2.97	920
LASC-P03-P10B	57.7	-0.01	28.1	0.26	0.04	9.4	5.59	0.50	0.10	46.6	50.4	2.96	920
LASC-P03-P11A	55.5	0.05	29.3	0.51	0.04	10.9	4.98	0.34	0.19	53.6	44.4	1.99	955
LASC-P03-P11B	52.7	0.04	31.1	0.53	0.05	12.9	3.87	0.24	-0.03	63.9	34.7	1.41	1006
LASC-P03-P11C	56.6	0.04	28.4	0.43	0.06	9.9	5.36	0.42	0.13	49.3	48.2	2.47	933

LASC-P03-P11D	54.5	0.00	29.9	0.48	0.05	11.5	4.53	0.30	-0.05	57.3	40.9	1.80	973
LASC-P03-P11E	53.2	0.06	30.8	0.44	0.04	12.7	3.98	0.23	-0.02	62.9	35.7	1.34	1002
LASC-P03-P11F	51.2	0.00	32.4	0.55	0.04	14.1	3.18	0.16	0.06	70.3	28.8	0.97	1038
LASC-P03-P11G	52.4	-0.01	31.1	0.51	0.04	13.0	3.76	0.20	0.12	64.9	33.8	1.21	1012
LASC-P03-P11H	54.5	0.03	30.2	0.52	0.06	11.9	4.40	0.29	0.06	58.9	39.4	1.70	981
LASC-P03-P11I	52.5	0.03	31.5	0.50	0.05	13.1	3.71	0.22	-0.01	65.2	33.4	1.33	1013
LASC-P03-P11J	54.7	0.05	30.0	0.52	0.05	11.7	4.50	0.30	0.11	58.0	40.2	1.76	977
LASC-P03-P12A	55.7	0.05	29.3	0.48	0.05	10.9	4.87	0.32	0.04	54.1	43.9	1.92	958
LASC-P03-P12B	54.9	0.05	29.8	0.49	0.04	11.5	4.61	0.29	-0.04	56.9	41.4	1.74	971
LASC-P03-P12C	57.8	-0.01	27.5	0.49	0.06	9.2	5.60	0.48	0.08	46.2	50.9	2.90	918
LASC-P03-P13A	55.6	0.07	29.5	0.45	0.04	10.9	4.95	0.36	0.07	53.8	44.1	2.11	956
LASC-P03-P13B	55.5	0.00	29.3	0.45	0.04	10.8	4.95	0.37	-0.04	53.6	44.2	2.19	955
LASC-P03-P13C	55.0	0.04	29.5	0.44	0.04	11.2	4.73	0.32	0.01	55.7	42.5	1.87	965
LASC-P03-P13D	53.4	0.01	30.5	0.46	0.05	12.1	4.13	0.25	0.03	61.0	37.5	1.49	992
LASC-P03-P13E	55.0	0.05	29.7	0.47	0.05	11.3	4.74	0.33	0.08	55.7	42.4	1.92	965
LASC-P03A-P1A	55.2	0.05	29.4	0.51	0.05	11.0	4.74	0.33	0.12	55.1	42.9	1.98	962

LASC-P03A-P1B	52.5	-0.02	31.3	0.53	0.05	13.2	3.85	0.22	0.01	64.6	34.1	1.27	1010
LASC-P03A-P1C	53.4	0.01	29.9	0.53	0.06	11.7	4.45	0.28	0.04	58.3	40.0	1.67	978
LASC-P03A-P1D	52.7	0.02	30.8	0.56	0.06	12.7	3.89	0.24	0.04	63.4	35.2	1.44	1004
LASC-P03A-P1E	53.1	0.02	29.6	0.52	0.06	11.7	4.42	0.26	-0.04	58.5	40.0	1.53	979
LASC-P03A-P1F	52.5	0.01	31.0	0.59	0.05	12.9	3.83	0.23	-0.10	64.2	34.4	1.35	1008
LASC-P03A-P1G	54.3	0.05	29.3	0.50	0.06	11.4	4.64	0.30	0.01	56.6	41.6	1.74	970
LASC-P03A-P1H	52.6	0.01	30.7	0.55	0.07	12.7	4.00	0.23	0.02	62.9	35.8	1.37	1001
LASC-P03A-P1I	54.7	0.03	29.7	0.51	0.06	11.5	4.53	0.30	0.05	57.4	40.8	1.79	974
LASC-P03A-P1J	53.9	0.04	30.1	0.56	0.05	11.8	4.49	0.30	0.04	58.3	40.0	1.74	978
LASC-P03A-P1K	54.2	0.05	30.1	0.55	0.07	11.8	4.44	0.29	0.01	58.4	39.9	1.71	979
LASC-P03A-P1KA	52.9	0.02	30.6	0.51	0.06	12.5	3.99	0.25	0.07	62.5	36.0	1.46	1000
LASC-P03A-P1KB	54.1	0.02	30.2	0.52	0.05	12.0	4.47	0.30	0.02	58.6	39.6	1.73	980
LASC-P03A-P1KC	53.2	0.03	30.5	0.53	0.06	12.4	4.22	0.25	0.10	61.0	37.6	1.46	992
LASC-P03A-P1KD	52.0	0.05	31.4	0.52	0.06	13.2	3.66	0.21	-0.02	65.8	33.0	1.25	1016
LASC-P03A-P1KE	52.1	0.04	31.4	0.51	0.06	13.3	3.62	0.20	0.01	66.2	32.6	1.19	1018
LASC-P03A-P1KF	52.5	0.03	30.9	0.55	0.05	12.8	3.86	0.21	0.02	63.9	34.8	1.27	1006

LASC-P03A-P1KG	55.1	0.02	28.9	0.52	0.07	11.1	4.72	0.36	0.07	55.4	42.5	2.11	964
LASC-P03A-P1KH	48.0	0.04	26.8	0.52	0.08	17.1	3.87	0.30	-0.02	69.9	28.6	1.47	1036
LASC-P03A-P1KI	54.4	0.04	29.5	0.57	0.06	11.4	4.60	0.29	-0.05	56.8	41.5	1.72	971
LASC-P03A-P1KJ	53.9	0.05	29.5	0.47	0.07	11.4	4.51	0.31	-0.13	57.3	40.9	1.84	973
LASC-P03A-P1KK	53.7	0.03	29.7	0.51	0.06	11.8	4.38	0.27	-0.01	58.9	39.5	1.60	981
LASC-P03A-P2A	54.3	0.06	29.8	0.44	0.06	11.6	4.48	0.30	0.02	57.8	40.4	1.79	976
LASC-P03A-P2B	52.2	-0.02	30.8	0.50	0.05	12.9	3.79	0.22	0.03	64.5	34.2	1.32	1009
LASC-P03A-P2C	55.3	0.01	29.0	0.50	0.05	10.7	4.94	0.39	0.08	53.3	44.3	2.33	953
LASC-P03A-P2D	51.8	0.02	31.2	0.57	0.04	13.2	3.63	0.22	-0.02	65.9	32.8	1.31	1016
LASC-P03A-P2E	54.0	-0.01	29.7	0.55	0.05	11.8	4.40	0.33	-0.05	58.5	39.5	1.95	979
LASC-P03A-P3A	54.9	0.01	30.1	0.37	0.05	11.5	4.66	0.31	-0.02	56.6	41.6	1.84	970
LASC-P03A-P3B	54.3	0.04	30.0	0.55	0.07	11.8	4.39	0.29	0.08	58.8	39.5	1.72	981
LASC-P03A-P3C	53.7	0.02	29.9	0.52	0.08	11.8	4.38	0.30	-0.04	58.8	39.4	1.76	981
LASC-P03A-P4A	54.9	-0.02	29.8	0.54	0.07	11.5	4.60	0.31	0.11	56.9	41.3	1.82	971
LASC-P03A-P4B	54.1	0.03	29.3	0.50	0.07	11.3	4.51	0.32	0.08	56.9	41.2	1.94	971
LASC-P03A-P4C	54.3	0.04	29.8	0.51	0.05	11.6	4.55	0.29	0.05	57.5	40.8	1.68	974

LASC-P03A-P4D	46.2	0.02	34.9	0.58	0.04	17.4	1.58	0.05	0.05	85.6	14.1	0.31	1115
LASC-P03A-P4E	54.0	0.05	29.8	0.52	0.07	11.7	4.59	0.28	0.04	57.4	40.9	1.64	974
LASC-P03A-P5A	51.6	0.03	31.1	0.54	0.05	13.2	3.78	0.22	0.08	65.0	33.7	1.28	1012
LASC-P03A-P5B	52.6	0.01	31.3	0.53	0.05	12.9	4.02	0.23	0.01	63.1	35.6	1.36	1002
LASC-P03A-P5C	53.9	0.03	29.2	0.52	0.06	11.4	4.60	0.31	0.08	56.6	41.5	1.82	970
LASC-P03A-P5D	53.0	0.04	30.1	0.52	0.06	12.1	4.33	0.28	-0.01	59.6	38.8	1.63	985
LASC-P03A-P5E	53.5	0.03	29.9	0.53	0.05	11.8	4.35	0.29	-0.08	58.9	39.4	1.71	981
LASC-P03A-P5F	55.3	0.01	29.0	0.53	0.07	10.9	4.97	0.34	0.02	53.6	44.4	1.98	955
LASC-P03A-P5G	55.3	0.02	29.2	0.52	0.06	10.9	4.87	0.34	0.05	54.1	43.9	2.01	957
LASC-P03A-P5H	54.8	0.01	29.1	0.52	0.06	10.9	4.88	0.35	-0.01	54.2	43.8	2.06	958
LASC-P03A-P5I	53.0	0.00	30.4	0.56	0.06	12.3	4.18	0.26	-0.04	61.0	37.5	1.53	992
LASC-P03A-P5J	52.3	0.02	31.1	0.55	0.05	13.1	3.80	0.24	-0.04	64.6	34.0	1.39	1010
LASC-P03A-P5K	54.5	0.04	29.4	0.56	0.06	11.4	4.73	0.32	0.05	56.0	42.1	1.87	967
LASC-P03A-P5L	54.4	0.02	29.5	0.51	0.07	11.3	4.60	0.31	0.03	56.6	41.5	1.84	970
LASC-P03A-P5LA	51.7	0.01	31.4	0.55	0.05	13.3	3.60	0.21	0.05	66.2	32.5	1.25	1018
LASC-P03A-P5LB	52.4	0.06	31.1	0.54	0.05	13.0	3.83	0.23	0.14	64.4	34.2	1.33	1009

LASC-P03A-P5LC	53.4	0.04	30.2	0.52	0.04	12.4	4.16	0.26	0.02	61.3	37.2	1.55	993
LASC-P03A-P5LD	54.2	0.07	29.6	0.51	0.06	11.5	4.60	0.32	-0.07	56.8	41.3	1.87	971
LASC-P03A-P5LE	53.4	0.03	29.5	0.54	0.06	11.8	4.36	0.28	0.08	59.0	39.3	1.67	982
LASC-P03A-P5LF	54.6	0.02	28.8	0.54	0.06	10.7	4.92	0.37	0.01	53.3	44.5	2.21	953
LASC-P03A-P5LG	50.6	0.04	31.4	0.56	0.06	13.5	3.52	0.21	0.10	67.1	31.7	1.23	1022
LASC-P03A-P5LH	53.9	-0.01	29.5	0.48	0.06	11.3	4.64	0.32	0.05	56.2	41.9	1.88	968
LASC-P03A-P5LI	54.5	0.00	29.2	0.51	0.06	11.3	4.69	0.31	0.09	56.2	42.0	1.82	968
LASC-P03A-P5LJ	54.2	0.03	29.1	0.55	0.05	11.3	4.71	0.32	-0.01	55.8	42.3	1.88	966
LASC-P03A-P5LK	54.4	0.02	29.4	0.50	0.06	11.2	4.71	0.32	0.06	55.8	42.3	1.89	966
LASC-P03A-P6A	46.6	-0.02	35.1	0.57	0.04	17.4	1.61	0.06	-0.08	85.4	14.3	0.37	1114
LASC-P03A-P6B	46.6	0.03	34.1	0.61	0.06	16.6	1.85	0.08	0.01	82.8	16.7	0.46	1101
LASC-P03A-P6C	46.9	0.03	34.7	0.64	0.04	17.1	1.75	0.07	-0.01	84.0	15.6	0.39	1107
LASC-P03A-P6D	50.8	0.04	31.6	0.62	0.06	13.7	3.42	0.19	-0.12	68.1	30.7	1.10	1028
LASC-P03A-P6E	53.7	0.08	29.7	0.66	0.09	11.7	4.42	0.31	0.01	58.2	39.9	1.83	978
LASC-P03A-P6F	53.0	0.03	29.2	0.59	0.07	11.6	4.34	0.28	0.00	58.7	39.7	1.69	980
LASC-P03A-P6G	53.3	0.04	30.3	0.63	0.07	12.2	4.23	0.26	0.13	60.6	37.9	1.51	990

LASC-P03A-P6H	52.4	0.05	30.4	0.71	0.07	12.5	3.98	0.24	0.04	62.5	36.1	1.42	999
LASC-P03A-P6I	54.7	0.04	29.2	0.60	0.08	11.3	4.65	0.35	-0.01	56.1	41.9	2.07	967
LASC-P03A-P6J	51.7	0.02	30.5	0.65	0.07	13.0	3.64	0.22	0.00	65.5	33.2	1.31	1014
LASC-P03A-P6K	52.8	0.02	30.3	0.64	0.08	12.4	4.13	0.25	0.02	61.5	37.1	1.46	994
LASC-P03A-P6L	53.4	0.06	30.5	0.63	0.07	12.3	4.17	0.26	0.06	61.0	37.4	1.54	992
LASC-P03A-P6M	50.9	0.05	32.0	0.66	0.07	14.0	3.30	0.19	0.01	69.3	29.6	1.10	1033
LASC-P03A-P6N	52.8	0.01	29.1	0.74	0.08	11.8	4.13	0.24	-0.02	60.4	38.1	1.45	989
LASC-P03A-P6O	52.6	0.05	30.5	0.69	0.07	12.7	3.98	0.23	0.01	63.0	35.7	1.33	1002
LASC-P03A-P6P	52.3	0.06	30.7	0.66	0.08	12.8	3.97	0.23	0.04	63.1	35.5	1.36	1002
LASC-P03A-P6Q	54.2	0.02	29.2	0.74	0.07	11.5	4.54	0.31	0.01	57.3	40.9	1.86	973
LASC-P03A-P7A	54.9	0.03	28.9	0.37	0.04	10.5	5.13	0.37	-0.11	51.8	46.0	2.18	946
LASC-P03A-P7B	53.9	0.04	29.5	0.54	0.06	11.3	4.70	0.31	0.05	56.1	42.1	1.81	967
LASC-P03A-P8A	52.5	0.01	30.8	0.51	0.03	12.6	4.05	0.26	0.05	62.4	36.1	1.54	999
LASC-P03A-P8B	53.8	0.00	29.7	0.52	0.05	11.4	4.60	0.35	-0.03	56.6	41.4	2.06	970
LASC-P03A-P8C	51.4	-0.01	31.9	0.55	0.05	13.7	3.35	0.19	0.02	68.6	30.3	1.14	1030
LASC-P03A-P8D	53.8	0.02	29.5	0.55	0.05	11.4	4.54	0.33	0.16	57.0	41.0	1.96	972

LASC-P03A-P8E	55.5	0.02	28.7	0.51	0.05	10.6	5.01	0.41	0.05	52.5	45.1	2.40	949
LASC-P03A-P8F	54.3	0.00	28.1	0.52	0.05	10.4	4.94	0.39	-0.06	52.4	45.2	2.33	949
LASC-P03A-P8G	53.7	-0.01	29.6	0.52	0.05	11.6	4.50	0.32	0.06	57.6	40.5	1.90	975
LASC-P03A-P8H	54.6	0.03	29.2	0.53	0.05	11.0	4.73	0.37	0.15	55.1	42.7	2.21	962
LASC-P03A-P8I	54.4	0.02	29.2	0.56	0.06	11.2	4.72	0.36	-0.07	55.4	42.5	2.14	964
LASC-P03A-P8J	54.8	0.02	27.8	0.50	0.05	10.0	5.09	0.44	0.10	50.6	46.7	2.65	940
LASC-P03A-P9A	57.1	0.01	27.0	0.37	0.05	9.0	5.59	0.52	-0.01	45.7	51.2	3.12	915
LASC-P03A-P9B	56.7	-0.01	27.8	0.40	0.06	9.5	5.57	0.47	-0.07	47.1	50.2	2.77	922
LASC-P03A-P9C	53.9	0.01	29.5	0.62	0.07	11.5	4.55	0.28	0.09	57.2	41.1	1.66	973
LASC-P03A-P9D	52.2	0.05	29.9	0.70	0.08	12.3	3.99	0.25	-0.04	62.0	36.5	1.53	997
LASC-P03A-P10A	53.4	0.02	29.7	0.54	0.05	11.5	4.48	0.32	0.00	57.6	40.5	1.93	975
LASC-P03A-P10B	50.1	0.06	32.5	0.61	0.05	14.5	2.97	0.15	0.01	72.3	26.7	0.91	1049
LASC-P03A-P10C	53.6	0.01	29.7	0.53	0.06	11.6	4.53	0.31	0.04	57.4	40.7	1.86	974
LASC-P03A-P10D	51.3	0.00	31.3	0.66	0.06	13.6	3.36	0.20	0.04	68.3	30.5	1.20	1029
LASC-P03A-P10E	54.7	0.01	29.2	0.59	0.07	11.2	4.73	0.34	0.01	55.4	42.5	2.04	964
LASC-P03A-P11A	53.8	-0.01	28.7	0.59	0.07	10.9	4.66	0.36	0.04	55.3	42.6	2.15	963

LASC-P03A-P11B	54.6	-0.02	29.5	0.56	0.08	11.4	4.63	0.30	0.01	56.5	41.7	1.80	969
LASC-P03A-P11C	53.9	0.02	29.5	0.60	0.06	11.5	4.55	0.31	0.04	57.2	41.0	1.84	973
LASC-P03A-P11D	54.0	0.00	29.3	0.62	0.07	11.1	4.72	0.32	0.03	55.4	42.7	1.93	964
LASC-P03A-P11E	56.1	0.04	27.6	0.57	0.09	9.6	5.43	0.45	-0.05	48.1	49.2	2.71	927
LASC-P03A-P11F	56.3	0.03	27.8	0.55	0.07	9.6	5.37	0.44	0.09	48.4	49.0	2.64	929
LASC-P03A-P11G	56.3	0.04	27.9	0.53	0.07	9.8	5.31	0.39	0.07	49.4	48.3	2.30	934
LASC-P03A-P11H	51.1	0.02	31.5	0.59	0.07	13.7	3.44	0.20	-0.06	67.9	31.0	1.19	1026
LASC-P03A-P11I	53.1	0.01	30.2	0.60	0.05	12.3	4.11	0.25	0.01	61.4	37.1	1.51	994
LASC-P03A-P11J	51.7	0.04	30.7	0.63	0.06	12.8	3.84	0.23	0.02	63.9	34.7	1.37	1006
LASC-P03A-P11K	53.3	0.08	29.3	0.62	0.07	11.5	4.47	0.30	0.03	57.6	40.5	1.82	975
LASC-P03A-P12A	57.1	-0.01	27.2	0.35	0.05	9.0	5.78	0.54	-0.04	44.7	52.1	3.20	910
LASC-P03A-P12B	52.3	0.05	30.3	0.60	0.07	12.2	4.19	0.28	0.05	60.8	37.6	1.65	991
LASC-P03A-P12C	62.9	0.41	19.7	2.46	0.71	5.7	4.19	2.43	-0.01	35.1	47.0	17.94	862
LASC-P03A-P12D	52.5	0.04	30.3	0.68	0.09	12.6	4.04	0.26	0.07	62.4	36.1	1.54	999
LASC-P03A-P13A	52.1	-0.02	30.1	0.59	0.07	12.2	4.12	0.27	0.02	61.1	37.3	1.62	992
LASC-P03A-P13B	49.5	0.01	32.3	0.52	0.06	14.5	3.07	0.15	0.00	71.7	27.5	0.88	1045

LASC-P03A-P13C	52.7	0.02	30.7	0.50	0.05	12.5	4.01	0.24	0.05	62.4	36.1	1.42	999
LASC-P03A-P13D	50.9	-0.02	30.9	0.52	0.05	13.2	3.47	0.20	0.03	67.0	31.8	1.20	1022
LASC-P03A-P13F	53.2	0.04	30.1	0.56	0.06	12.0	4.31	0.27	0.14	59.7	38.7	1.62	985
LASC-P03A-P13G	52.3	0.03	30.2	0.57	0.07	12.2	4.17	0.24	-0.05	61.0	37.6	1.45	992
LASC-P03A-P14A	49.1	0.09	32.0	1.11	0.34	14.9	2.52	0.30	0.02	75.2	23.0	1.79	1063
LASC-P03A-P14B	47.3	0.00	33.6	0.62	0.08	15.9	2.19	0.07	-0.10	79.7	19.9	0.39	1085
LASC-P03A-P15A	52.4	0.01	30.6	0.55	0.06	12.6	4.00	0.24	0.01	62.6	36.0	1.45	1000
LASC-P03A-P15B	55.0	0.01	29.3	0.45	0.05	10.9	4.99	0.38	0.07	53.4	44.4	2.20	954
LASC-P03A-P15C	54.4	0.04	28.8	0.48	0.04	10.7	4.89	0.38	0.04	53.4	44.3	2.25	954
LASC-P03A-P15D	54.5	0.03	29.3	0.49	0.06	10.7	4.85	0.37	0.09	53.8	44.0	2.23	956
LASC-P03A-P15E	48.6	0.05	25.8	0.42	0.04	10.4	3.95	0.27	0.00	58.1	40.1	1.81	977
LASC-P03A-P15F	52.9	0.06	30.0	0.49	0.04	11.9	4.27	0.29	0.00	59.6	38.7	1.70	985
LASC-P03A-P15G	54.2	0.02	28.5	0.46	0.05	10.4	5.02	0.40	0.01	52.0	45.6	2.42	947
LASC-P03A-P15H	53.7	0.06	28.8	0.49	0.04	10.6	4.84	0.36	-0.04	53.5	44.3	2.18	954
LASC-P03A-P15I	50.4	0.00	31.6	0.61	0.05	13.9	3.39	0.19	-0.02	68.6	30.3	1.12	1030
LASC-P03A-P16A	47.1	0.01	34.2	0.55	0.07	16.6	2.12	0.07	-0.04	80.9	18.7	0.40	1091

LASC-P03A-P16B	46.3	0.03	34.8	0.52	0.07	17.1	1.74	0.06	-0.04	84.2	15.5	0.34	1108
LASC-P03A-P16C	48.3	-0.01	34.1	0.63	0.07	16.5	2.04	0.07	-0.02	81.4	18.1	0.41	1094
LASC-P03A-P17A	57.5	0.02	27.5	0.44	0.06	9.2	5.55	0.48	0.08	46.4	50.7	2.89	919
LASC-P03A-P17B	57.4	0.00	27.5	0.50	0.06	9.2	5.46	0.47	0.01	47.0	50.2	2.86	922
LASC-P03A-P17C	56.1	0.03	28.4	0.52	0.08	10.2	5.16	0.37	0.08	51.1	46.7	2.22	942
LASC-P03A-P18A	53.1	0.04	30.4	0.59	0.07	12.6	4.01	0.23	0.05	62.5	36.1	1.38	999
LASC-P03A-P18B	52.5	0.00	31.4	0.62	0.05	13.3	3.75	0.21	0.03	65.4	33.4	1.22	1014
LASC-P03A-P18C	51.7	-0.01	31.5	0.57	0.06	13.6	3.43	0.19	0.04	67.9	31.0	1.13	1026
LASC-P03A-P18D	52.2	0.07	31.4	0.51	0.06	13.4	3.57	0.20	0.04	66.6	32.2	1.20	1020
LASC-P03A-P18E	51.8	0.04	31.2	0.54	0.06	13.5	3.46	0.19	0.02	67.6	31.3	1.11	1025
LASC-P03A-P18F	55.2	0.03	29.2	0.54	0.08	11.2	4.66	0.33	0.10	56.0	42.0	1.93	967
LASC-P03A-P18G	54.9	0.03	29.2	0.62	0.07	11.1	4.71	0.35	-0.05	55.3	42.6	2.11	963
LASC-P03A-P18H	53.8	0.01	30.1	0.71	0.08	12.3	4.12	0.24	0.05	61.4	37.2	1.41	994
LASC-P03A-P18I	53.5	0.03	30.2	0.67	0.08	12.1	4.30	0.26	-0.04	59.9	38.5	1.52	987
LASC-P03A-P18J	53.1	0.00	30.6	0.67	0.08	12.7	3.97	0.24	-0.07	63.0	35.5	1.42	1002
LASC-P03A-P19A	54.2	0.02	29.9	0.54	0.05	11.8	4.32	0.30	0.02	59.2	39.0	1.80	983

LASC-P03A-P19B	50.4	-0.03	32.8	0.60	0.04	14.9	2.83	0.16	0.05	73.7	25.4	0.97	1055
LASC-P03A-P19C	50.6	0.04	32.7	0.58	0.04	14.7	2.97	0.17	0.00	72.5	26.5	0.98	1049
LASC-P03A-P19D	51.4	0.06	31.6	0.54	0.05	13.7	3.36	0.20	0.04	68.5	30.3	1.19	1029
LASC-P03A-P19E	53.8	0.02	30.1	0.50	0.05	12.0	4.17	0.28	0.04	60.3	38.0	1.67	988
LASC-P03A-P19F	55.2	0.03	29.1	0.56	0.05	10.9	4.75	0.34	0.09	54.9	43.1	2.01	961
LASC-P02-P1	48.6	0.03	34.3	0.68	0.06	16.4	2.23	0.14	0.03	79.6	19.6	0.78	1085
LASC-P02-P1B	48.5	0.01	33.3	0.55	0.03	15.7	2.37	0.14	-0.02	77.9	21.3	0.81	1077
LASC-P02-P2B	49.4	0.00	32.9	0.55	0.02	15.0	2.73	0.17	0.13	74.5	24.5	1.01	1059
LASC-P02-P3A	56.6	-0.02	27.5	0.36	0.03	9.3	5.51	0.61	-0.06	46.5	49.9	3.62	919
LASC-P02-P3B	56.4	0.01	27.8	0.36	0.03	9.3	5.50	0.59	0.16	46.5	50.0	3.53	919
LASC-P02-P4A	53.7	0.02	28.6	0.32	0.04	10.3	4.79	0.44	0.02	52.8	44.5	2.70	951
LASC-P02-P4B	51.8	0.01	30.2	0.41	0.04	12.1	4.02	0.32	0.06	61.2	36.9	1.95	993
LASC-P02-P4C	55.4	-0.02	27.7	0.33	0.02	9.2	5.35	0.53	0.09	47.2	49.5	3.25	923
LASC-P02-P4D	50.8	0.04	30.4	0.55	0.04	12.4	3.71	0.29	0.02	63.7	34.5	1.79	1006
LASC-P02-P4AA	54.9	-0.01	29.4	0.24	0.02	11.0	4.80	0.41	0.01	54.4	43.1	2.45	959
LASC-P02-P4AB	56.2	-0.01	29.5	0.21	0.03	10.8	4.90	0.43	0.01	53.4	44.0	2.53	954

LASC-P02-P4AC	56.1	0.01	28.4	0.27	0.04	9.8	5.17	0.52	0.03	49.5	47.4	3.13	934
LASC-P02-P4AD	56.8	0.04	27.1	0.24	0.03	9.0	5.58	0.59	0.03	45.5	51.0	3.52	914
LASC-P02-P4AE	56.7	0.01	28.3	0.28	0.04	9.6	5.41	0.52	0.04	48.1	48.8	3.07	927
LASC-P02-P4AF	55.7	-0.03	29.0	0.31	0.05	10.3	5.14	0.47	-0.06	51.0	46.2	2.79	942
LASC-P02-P4AG	56.0	0.00	28.4	0.31	0.04	10.0	5.35	0.51	-0.01	49.3	47.7	2.97	933
LASC-P02-P4AH	55.4	0.05	28.0	0.54	0.06	10.0	5.08	0.54	0.05	50.3	46.4	3.26	938
LASC-P02-P4AI	53.5	0.00	29.9	0.44	0.06	11.7	4.38	0.32	-0.01	58.4	39.7	1.93	979
LASC-P02-P4ABA	56.6	-0.01	27.2	0.21	0.03	9.1	5.41	0.58	0.04	46.5	50.0	3.52	919
LASC-P02-P4ABB	55.3	0.01	29.2	0.27	0.03	10.8	4.97	0.47	0.01	53.2	44.1	2.77	953
LASC-P02-P4ABC	57.2	0.01	27.8	0.22	0.02	9.2	5.66	0.61	0.01	45.6	50.9	3.58	915
LASC-P02-P4ABD	57.5	0.00	27.8	0.21	0.03	9.1	5.76	0.59	0.10	45.1	51.5	3.48	912
LASC-P02-P4ABE	57.2	0.04	27.5	0.27	0.04	9.0	5.65	0.60	-0.15	45.1	51.3	3.60	912
LASC-P02-P4ABF	57.5	0.04	27.2	0.38	0.04	8.9	5.79	0.65	0.07	44.1	52.1	3.86	907
LASC-P02-P4ABG	55.4	0.02	28.5	0.59	0.04	10.4	4.99	0.51	-0.02	51.8	45.2	3.04	946
LASC-P02-P46A	49.4	0.00	33.3	0.62	0.03	15.3	2.63	0.17	-0.02	75.6	23.4	1.00	1065
LASC-P02-P6B	50.0	0.03	32.9	0.61	0.04	15.0	2.77	0.17	-0.04	74.3	24.7	1.00	1058

LASC-P02-P6C	51.8	0.01	31.0	0.54	0.04	13.1	3.70	0.26	0.02	65.2	33.3	1.54	1013
LASC-P02-P6D	54.4	-0.02	29.2	0.72	0.05	11.2	4.73	0.44	-0.09	55.3	42.1	2.56	963
LASC-P02-P7A	57.2	-0.01	27.6	0.39	0.03	9.3	5.52	0.63	0.17	46.5	49.8	3.73	919
LASC-P02-P7B	57.7	0.01	27.4	0.44	0.02	8.8	5.75	0.68	0.03	44.0	52.0	4.05	907
LASC-P02-P7C	51.4	0.02	31.6	0.45	0.03	13.7	3.42	0.25	0.01	68.0	30.6	1.49	1027
LASC-P02-P7D	52.7	0.04	30.6	0.65	0.03	12.8	3.89	0.31	0.07	63.4	34.8	1.82	1004
LASC-P02-P8A	49.5	0.03	33.5	0.46	0.01	15.6	2.49	0.16	0.09	76.9	22.1	0.92	1072
LASC-P02-P8B	55.6	0.02	28.9	0.39	0.02	10.4	5.05	0.50	0.06	51.5	45.5	2.99	944
LASC-P02-P8C	53.9	0.10	29.2	0.59	0.04	11.4	4.47	0.45	0.05	57.0	40.3	2.68	972
LASC-P02-P9A	50.2	0.03	32.2	0.62	0.03	14.6	2.86	0.20	0.04	73.0	25.9	1.19	1052
LASC-P02-P10A	60.0	0.01	25.4	0.42	0.02	7.0	6.58	0.98	0.11	34.7	59.4	5.83	861
LASC-P02-P10B	58.5	0.03	26.7	0.39	0.03	8.1	6.06	0.76	0.08	40.5	54.9	4.54	889
LASC-P03B-P2	48.0	0.02	34.1	0.63	0.08	16.5	2.10	0.09	-0.06	80.8	18.7	0.51	1091
LASC-P03B-P3	54.4	0.05	30.3	0.52	0.06	12.1	4.29	0.29	0.04	59.9	38.4	1.70	987
LASC-P03B-P4A	51.1	0.04	31.5	0.64	0.07	13.9	3.28	0.18	-0.04	69.2	29.7	1.09	1033
LASC-P03B-P4B	54.6	0.01	29.3	0.62	0.07	11.4	4.55	0.31	-0.05	57.0	41.2	1.83	972

LASC-P03B-P4C	53.7	0.01	29.6	0.58	0.07	11.7	4.45	0.30	0.04	58.3	40.0	1.76	978
LASC-P03B-P4D	54.8	0.06	29.3	0.72	0.07	11.3	4.59	0.32	-0.04	56.5	41.5	1.92	970
LASC-P03B-P5A	52.8	0.03	30.7	0.51	0.07	12.4	4.10	0.24	0.11	61.7	36.8	1.43	996

Appendix A-2. Pyroxene major element concentrations and end member compositions for single crystals from multiple samples.

	Weight %										End Member		
Name	SiO_2	TiO_2	Al_2O_3	Cr_2O_3	FeO	MnO	MgO	CaO	Na_2O	NiO	%Wo	%En	%Fs
LC 24-04 Pyroxene 1a	52.47	0.39	1.76	-0.05	8.96	0.29	15.03	21.37	0.40	0.02	43.37	42.44	14.20
LC 24-04 Pyroxene 1b	52.39	0.36	1.77	-0.01	8.84	0.30	15.12	21.28	0.37	0.02	43.24	42.74	14.03
LC 24-04 Pyroxene 1c	52.46	0.37	1.73	0.01	9.05	0.32	15.28	21.15	0.37	-0.04	42.75	42.97	14.27
LC 24-04 Pyroxene 1A	51.82	0.56	2.68	0.02	9.21	0.26	14.71	21.13	0.41	0.04	43.31	41.96	14.73
LC 24-04 Pyroxene 1B	52.05	0.47	2.51	0.01	9.08	0.26	14.78	21.13	0.44	-0.02	43.31	42.16	14.53
LC 24-04 Pyroxene 1C	51.90	0.45	2.41	-0.01	9.19	0.27	14.68	21.22	0.49	0.01	43.47	41.85	14.69
LC 24-04 Pyroxene 2a	54.62	0.14	0.63	0.01	17.95	0.56	25.97	1.19	0.01	0.06	2.32	70.38	27.30
LC 24-04 Pyroxene 2b	54.39	0.16	0.53	-0.03	17.55	0.49	25.83	1.15	0.02	0.01	2.26	70.78	26.97
LC 24-04 Pyroxene 2c	54.39	0.13	0.47	0.04	17.72	0.47	26.17	1.11	0.04	0.01	2.16	70.90	26.94

LC 24-04 Pyroxene 2A	53.40	0.22	1.43	-0.01	18.06	0.46	25.09	1.20	0.03	-0.01	2.39	69.54	28.07
LC 24-04 Pyroxene 2B	53.45	0.25	1.16	0.02	18.35	0.56	25.34	1.15	0.04	-0.01	2.28	69.50	28.23
LC 24-04 Pyroxene 3a	53.75	0.22	1.66	-0.01	17.59	0.54	26.15	1.02	0.00	-0.01	2.00	71.16	26.84
LC 24-04 Pyroxene 3b	53.27	0.24	1.70	0.01	17.76	0.53	26.08	1.04	0.04	0.03	2.04	70.89	27.07
LC 24-04 Pyroxene 3c	53.45	0.25	1.80	0.02	17.79	0.61	25.74	0.99	0.00	-0.02	1.96	70.66	27.39
LC 24-04 Pyroxene 3A	54.49	0.17	0.78	0.01	18.43	0.56	25.28	1.14	0.02	-0.01	2.26	69.37	28.37
LC 24-04 Pyroxene 3B	54.80	0.18	0.58	0.00	17.73	0.55	25.35	1.11	0.02	0.05	2.22	70.23	27.55
LC 24-04 Pyroxene 3C	53.80	0.15	0.97	-0.03	18.63	0.59	25.06	1.14	0.04	-0.06	2.25	68.99	28.76
LC 24-04 Pyroxene 4a	53.87	0.25	1.46	-0.01	18.00	0.39	25.51	1.30	0.04	0.06	2.55	69.82	27.63
LC 24-04 Pyroxene 4b	53.46	0.25	1.52	-0.05	17.87	0.40	25.63	1.29	0.02	0.01	2.53	70.06	27.41
LC 24-04 Pyroxene 4c	53.33	0.27	1.51	0.00	17.77	0.38	25.61	1.26	0.03	-0.01	2.49	70.20	27.32
LC 24-04 Pyroxene 4A	53.47	0.18	1.13	-0.02	17.95	0.44	25.62	1.17	-0.01	-0.05	2.30	70.13	27.56
LC 24-04 Pyroxene 4B	53.45	0.20	1.32	0.01	18.14	0.48	25.42	1.13	0.02	0.03	2.23	69.82	27.94
LC 24-04 Pyroxene 4C	53.23	0.16	1.34	0.02	18.71	0.51	25.13	1.12	0.05	0.00	2.21	68.98	28.81
LC 24-04 Pyroxene 5a	52.93	0.23	1.93	-0.02	18.44	0.61	25.26	0.88	0.04	-0.03	1.74	69.71	28.55
LC 24-04 Pyroxene 5b	52.91	0.24	1.90	-0.02	18.32	0.63	25.00	0.92	0.00	-0.03	1.85	69.56	28.59

LC 24-04 Pyroxene 5c	52.69	0.19	2.04	-0.01	18.34	0.66	25.23	0.88	0.02	-0.01	1.74	69.80	28.46
LC 24-04 Pyroxene 5A	54.90	6.89	14.05	0.00	16.41	0.01	0.88	2.81	3.57	-0.01	16.71	7.27	76.02
LC 24-04 Pyroxene 5B	54.09	0.19	1.22	-0.05	18.39	0.53	25.39	1.07	0.02	-0.03	2.12	69.61	28.27
LC 24-04 Pyroxene 5C	53.73	0.21	1.24	-0.01	18.20	0.54	25.32	1.06	0.04	0.02	2.10	69.77	28.13
LC 24-04 Pyroxene 6a	54.46	0.14	0.60	0.00	17.47	0.57	26.21	1.15	0.04	-0.01	2.24	71.15	26.61
LC 24-04 Pyroxene 6b	54.50	0.15	0.63	-0.01	17.45	0.54	26.15	1.17	0.02	0.03	2.29	71.10	26.62
LC 24-04 Pyroxene 6c	54.77	0.17	0.73	-0.02	17.46	0.59	26.28	1.16	0.02	0.03	2.27	71.20	26.54
LC 24-04 Pyroxene 6A	54.06	0.22	1.52	0.01	16.72	0.43	25.62	1.27	0.00	0.01	2.55	71.35	26.11
LC 24-04 Pyroxene 6B	53.18	0.25	3.17	0.16	14.34	0.17	27.64	1.53	0.05	0.05	2.99	75.14	21.87
LC 24-04 Pyroxene 6C	53.86	0.25	1.30	0.02	16.98	0.43	26.44	1.27	0.03	0.03	2.47	71.70	25.82
LC 24-04 Pyroxene 7a	52.77	0.32	2.93	0.02	18.87	0.36	24.56	1.40	0.02	-0.01	2.78	67.94	29.28
LC 24-04 Pyroxene 7b	52.06	0.30	2.88	-0.02	18.85	0.37	24.45	1.41	0.03	0.02	2.81	67.85	29.34
LC 24-04 Pyroxene 7c	52.10	0.33	2.89	0.04	18.59	0.40	24.46	1.42	0.03	0.03	2.85	68.12	29.03
LC 24-04 Pyroxene 7A	52.34	0.35	1.57	0.00	8.94	0.37	15.61	20.65	0.36	0.02	41.85	44.01	14.14
LC 24-04 Pyroxene 7B	52.86	0.35	1.58	0.00	9.24	0.33	15.81	20.43	0.31	-0.01	41.15	44.33	14.53
LC 24-04 Pyroxene 7C	49.87	0.39	2.03	-0.01	8.25	0.29	14.52	19.76	0.24	-0.01	42.58	43.54	13.88

LC 24-04 Pyroxene 8a	53.64	0.18	1.05	-0.02	18.95	0.59	25.17	1.19	0.03	0.00	2.33	68.68	28.99
LC 24-04 Pyroxene 8b	53.96	0.16	1.01	-0.04	18.87	0.60	24.96	1.16	0.03	-0.04	2.29	68.63	29.09
LC 24-04 Pyroxene 8c	53.66	0.23	1.14	0.00	18.81	0.56	24.93	1.14	0.04	-0.04	2.25	68.69	29.06
LC 24-04 Pyroxene 8A	53.36	0.27	1.78	0.00	18.57	0.46	25.09	1.20	0.03	0.00	2.36	69.00	28.64
LC 24-04 Pyroxene 8B	53.44	0.22	1.22	0.03	18.06	0.48	25.03	1.21	0.02	-0.07	2.42	69.47	28.11
LC 24-04 Pyroxene 8C	54.27	0.21	1.10	-0.01	18.35	0.53	25.52	1.12	0.03	0.08	2.20	69.69	28.10
LC 24-04 Pyroxene 9a	53.06	0.24	1.95	0.00	17.91	0.54	25.15	1.23	0.03	0.01	2.45	69.71	27.84
LC 24-04 Pyroxene 9b	53.37	0.22	1.53	0.02	17.97	0.53	25.70	1.09	0.01	0.01	2.13	70.30	27.57
LC 24-04 Pyroxene 9c	53.76	0.25	1.79	0.00	18.33	0.55	25.70	1.11	0.03	-0.02	2.17	69.87	27.96
LC 24-04 Pyroxene 9A	53.94	0.24	1.38	0.01	19.34	0.51	24.37	1.25	0.07	0.00	2.49	67.47	30.04
LC 24-04 Pyroxene 9B	53.49	0.25	1.64	0.03	18.54	0.55	25.00	1.12	0.04	-0.02	2.22	69.06	28.72
LC 24-04 Pyroxene 9C	53.68	0.20	1.51	0.00	18.23	0.57	25.24	1.06	0.02	-0.01	2.10	69.67	28.23
LC 24-04 Pyroxene 10a	53.65	0.27	1.81	0.00	17.51	0.40	25.70	1.27	0.02	0.01	2.50	70.54	26.96
LC 24-04 Pyroxene 10b	53.93	0.28	1.65	-0.01	17.51	0.35	25.74	1.26	0.03	0.00	2.49	70.57	26.94
LC 24-04 Pyroxene 10c	53.34	0.28	2.08	0.01	17.52	0.32	25.58	1.31	0.03	0.04	2.59	70.37	27.04
LC 24-04 Pyroxene 10A	64.13	0.24	20.63	-0.03	1.29	0.00	0.30	4.54	6.66	-0.01	76.10	7.01	16.89

LC 24-04 Pyroxene 10B	53.76	0.22	1.17	0.01	17.99	0.46	25.05	1.10	0.04	0.00	2.20	69.71	28.08
LC 24-04 Pyroxene 10C	52.92	0.31	2.24	0.02	18.30	0.37	25.01	1.25	0.02	0.00	2.49	69.14	28.38
LC 25-05 Pyroxene 1a	53.89	0.13	1.09	0.00	19.25	0.52	24.67	1.08	0.00	-0.05	2.15	68.07	29.79
LC 25-05 Pyroxene 1b	53.99	0.17	0.90	-0.01	19.22	0.49	24.99	1.03	0.03	0.05	2.02	68.45	29.53
LC 25-05 Pyroxene 1c	53.71	0.15	0.99	0.04	19.23	0.50	24.87	1.11	0.01	0.02	2.19	68.22	29.59
LC 25-05 Pyroxene 1A	55.28	0.24	0.94	0.00	13.63	0.41	28.80	1.35	0.03	0.01	2.60	76.97	20.43
LC 25-05 Pyroxene 1B	55.18	0.21	0.83	0.04	13.58	0.37	28.43	1.43	0.00	0.03	2.77	76.69	20.54
LC 25-05 Pyroxene 1C	54.85	0.28	1.39	0.02	14.21	0.34	28.13	1.39	-0.01	0.01	2.69	75.82	21.49
LC 25-05 Pyroxene 2a	51.26	0.79	3.30	-0.02	8.90	0.23	15.09	20.92	0.33	0.02	42.82	42.96	14.22
LC 25-05 Pyroxene 2b	52.25	0.55	2.16	-0.01	8.22	0.29	15.51	20.86	0.45	0.08	42.69	44.17	13.14
LC 25-05 Pyroxene 2c	50.76	0.98	3.50	0.03	9.38	0.28	15.02	20.64	0.40	0.02	42.24	42.77	14.99
LC 25-05 Pyroxene 2A	52.09	0.55	2.41	0.00	8.11	0.27	15.41	21.17	0.40	0.02	43.26	43.81	12.93
LC 25-05 Pyroxene 2B	51.82	0.70	2.56	0.02	8.12	0.24	15.46	21.05	0.38	0.04	43.05	43.98	12.97
LC 25-05 Pyroxene 2C	51.07	0.86	3.19	0.01	8.05	0.24	15.63	21.22	0.34	0.01	43.08	44.16	12.75
LC 25-05 Pyroxene 3a	52.59	0.27	1.27	0.02	19.68	0.42	23.61	1.23	0.03	0.00	2.48	66.45	31.06
LC 25-05 Pyroxene 3b	53.21	0.27	1.25	0.00	19.98	0.46	24.11	1.26	0.03	0.01	2.51	66.55	30.94

LC 25-05 Pyroxene 3c	53.26	0.26	1.25	0.02	19.87	0.47	23.81	1.30	0.04	-0.03	2.59	66.35	31.06
LC 25-05 Pyroxene 3A	54.52	0.31	1.21	0.02	15.78	0.42	27.31	1.36	0.02	0.06	2.63	73.54	23.83
LC 25-05 Pyroxene 3B	54.28	0.34	1.72	-0.02	15.74	0.42	27.26	1.43	0.04	0.03	2.77	73.44	23.79
LC 25-05 Pyroxene 3C	54.99	0.24	1.19	-0.01	15.36	0.41	27.55	1.25	0.03	0.02	2.43	74.33	23.25
LC 25-05 Pyroxene 4a	52.81	0.56	2.13	-0.03	8.09	0.21	15.69	21.40	0.39	0.03	43.19	44.07	12.74
LC 25-05 Pyroxene 4b	52.96	0.59	2.15	0.01	8.25	0.21	15.64	21.48	0.39	-0.01	43.24	43.80	12.96
LC 25-05 Pyroxene 4c	53.14	0.47	1.81	-0.03	8.34	0.26	16.26	21.10	0.31	0.03	42.00	45.04	12.95
LC 25-05 Pyroxene 4A	52.81	1.48	3.11	0.00	8.80	0.31	14.66	18.84	0.55	0.02	40.86	44.24	14.90
LC 25-05 Pyroxene 4B	50.11	1.09	3.94	0.03	9.32	0.28	14.99	20.29	0.34	-0.03	41.90	43.09	15.02
LC 25-05 Pyroxene 4C	51.34	0.82	3.39	0.01	9.10	0.27	15.52	20.88	0.34	0.03	42.11	43.56	14.33
LC 25-05 Pyroxene 5a	51.70	0.80	2.63	0.00	8.56	0.29	15.37	21.18	0.39	0.04	43.00	43.44	13.56
LC 25-05 Pyroxene 5b	52.17	0.73	2.46	-0.04	8.58	0.20	15.33	21.49	0.38	0.02	43.40	43.07	13.53
LC 25-05 Pyroxene 5c	51.97	0.82	2.74	0.01	8.88	0.22	15.24	21.30	0.37	0.03	43.08	42.89	14.02
LC 25-05 Pyroxene 5A	51.89	0.74	2.70	-0.02	8.12	0.25	15.50	21.18	0.30	-0.01	43.14	43.95	12.92
LC 25-05 Pyroxene 5B	51.66	0.78	2.83	0.02	8.16	0.18	15.24	21.41	0.33	-0.01	43.70	43.30	13.01
LC 25-05 Pyroxene 5C	49.54	0.87	3.31	0.01	8.41	0.26	14.56	20.68	0.35	0.08	43.53	42.64	13.82

LC 25-05 Pyroxene 6a	54.79	0.23	0.98	-0.01	16.24	0.38	26.92	1.14	0.03	0.04	2.23	73.05	24.72
LC 25-05 Pyroxene 6b	54.24	0.26	1.19	0.01	16.56	0.38	26.62	1.25	0.04	0.01	2.43	72.33	25.24
LC 25-05 Pyroxene 6c	54.60	0.24	1.02	0.02	16.46	0.38	26.53	1.19	0.01	0.02	2.33	72.45	25.22
LC 25-05 Pyroxene 6A	54.19	0.28	1.40	-0.03	16.01	0.42	26.72	1.36	0.03	0.02	2.66	72.85	24.49
LC 25-05 Pyroxene 6B	53.97	0.26	1.35	-0.02	16.21	0.41	26.75	1.33	0.02	-0.01	2.61	72.70	24.70
LC 25-05 Pyroxene 6C	53.96	0.31	1.48	-0.04	16.29	0.40	26.58	1.28	0.03	0.02	2.51	72.55	24.94
LC 25-05 Pyroxene 7a	52.87	0.53	1.80	0.02	8.04	0.22	15.91	20.96	0.33	0.01	42.45	44.83	12.71
LC 25-05 Pyroxene 7b	53.05	0.53	1.91	0.02	7.95	0.22	15.92	21.56	0.34	0.02	43.19	44.38	12.43
LC 25-05 Pyroxene 7c	53.05	0.50	1.67	-0.02	7.85	0.22	16.56	21.09	0.24	0.02	41.97	45.84	12.19
LC 25-05 Pyroxene 7A	53.25	0.41	1.50	0.00	7.76	0.21	16.69	20.55	0.25	-0.02	41.24	46.61	12.15
LC 25-05 Pyroxene 7B	52.05	0.64	2.45	0.00	8.19	0.24	15.15	21.39	0.37	0.01	43.78	43.14	13.08
LC 25-05 Pyroxene 7C	52.74	0.58	1.98	0.02	7.78	0.23	15.86	21.42	0.34	-0.01	43.21	44.53	12.26
LC 25-05 Pyroxene 8a	53.37	0.52	1.57	0.03	8.62	0.31	16.99	19.56	0.30	0.03	39.17	47.35	13.47
LC 25-05 Pyroxene 8b	52.41	0.59	2.01	0.02	8.66	0.25	16.48	20.27	0.40	0.04	40.57	45.90	13.53
LC 25-05 Pyroxene 8c	53.55	0.45	1.79	-0.01	10.39	0.24	19.31	14.90	0.25	0.02	29.87	53.88	16.25
LC 25-05 Pyroxene 8A	50.37	1.12	4.20	-0.01	9.26	0.19	14.86	21.04	0.35	-0.02	42.98	42.25	14.76

LC 25-05 Pyroxene 8B	51.12	0.82	3.22	0.01	8.57	0.18	15.03	21.66	0.32	-0.04	43.96	42.45	13.58
LC 25-05 Pyroxene 8C	51.33	0.90	3.03	-0.01	8.45	0.19	15.31	21.06	0.37	0.01	43.02	43.52	13.46
LC 25-05 Pyroxene 9a	52.10	0.63	2.40	0.00	8.14	0.26	15.42	21.44	0.43	0.02	43.54	43.56	12.90
LC 25-05 Pyroxene 9b	50.54	1.39	3.86	0.02	8.79	0.24	14.41	21.18	0.49	0.00	44.03	41.70	14.27
LC 25-05 Pyroxene 9c	50.59	1.28	3.69	-0.02	8.81	0.20	14.43	21.24	0.44	0.05	44.06	41.66	14.27
LC 25-05 Pyroxene 9A	51.42	0.81	2.98	0.02	8.14	0.23	15.51	21.27	0.32	0.01	43.22	43.87	12.91
LC 25-05 Pyroxene 9B	51.36	0.83	3.15	0.04	8.29	0.23	15.78	20.83	0.32	-0.04	42.29	44.58	13.14
LC 25-05 Pyroxene 9C	51.54	0.74	3.03	0.03	9.07	0.19	15.50	20.18	0.35	0.06	41.33	44.17	14.51
LC 25-05 Pyroxene 10a	53.22	0.11	1.12	-0.01	21.26	0.45	24.03	0.55	0.02	0.01	1.09	66.11	32.81
LC 25-05 Pyroxene 10b	53.23	0.08	1.10	0.00	21.16	0.45	23.77	0.53	0.02	0.05	1.05	65.99	32.95
LC 25-05 Pyroxene 10c	53.64	0.06	1.09	0.00	21.16	0.46	23.77	0.57	0.03	0.00	1.15	65.94	32.92
LC 25-05 Pyroxene 10A	53.07	0.09	1.40	-0.01	21.81	0.50	23.35	0.64	0.04	0.04	1.27	64.79	33.94
LC 25-05 Pyroxene 10B	53.16	0.06	1.37	-0.03	21.65	0.50	23.27	0.62	0.01	0.08	1.24	64.90	33.86
LC 25-05 Pyroxene 10C	52.40	0.09	1.50	-0.02	21.59	0.45	23.17	0.70	0.02	0.03	1.41	64.74	33.85

Appendix A-3. Pyroxene temperature and pressure data for Stage I samples from Putirka et al., 2008.

Orthopyroxene and Clinopyroxene Temperature – Pressure – Depth Stage I

Sample	Temperature (°C)	Pressure (kbar)	Depth (km)
LC 24-04 Pyroxene 2c	1052	0.3	1.3
LC 24-04 Pyroxene 2A	1056	0.9	3.5
LC 24-04 Pyroxene 2B	1053	0.5	1.9
LC 24-04 Pyroxene 3b	1055	0.8	2.9
LC 24-04 Pyroxene 3C	1055	0.8	3.0
LC 24-04 Pyroxene 4a	1056	0.9	3.5
LC 24-04 Pyroxene 4c	1052	0.4	1.6
LC 24-04 Pyroxene 4C	1056	1.0	3.6
LC 24-04 Pyroxene 5a	1059	1.2	4.7
LC 24-04 Pyroxene 5c	1050	0.1	0.4
LC 24-04 Pyroxene 5B	1049	0.0	0.1
LC 24-04 Pyroxene 5C	1056	0.9	3.3
LC 24-04 Pyroxene 6a	1051	0.3	1.2
LC 24-04 Pyroxene 6B	1062	1.7	6.4
LC 24-04 Pyroxene 7a	1056	1.0	3.7
LC 24-04 Pyroxene 7b	1062	1.7	6.3
LC 24-04 Pyroxene 7c	1061	1.6	6.1
LC 24-04 Pyroxene 7A	1091	5.8	21.9
LC 24-04 Pyroxene 7B	1088	5.4	20.5

LC 24-04 Pyroxene 7C	1092	6.1	23.0
LC 24-04 Pyroxene 8a	1050	0.1	0.5
LC 24-04 Pyroxene 8b	1054	0.7	2.6
LC 24-04 Pyroxene 8c	1057	1.0	3.8
LC 24-04 Pyroxene 8A	1054	0.6	2.3
LC 24-04 Pyroxene 8B	1050	0.2	0.8
LC 24-04 Pyroxene 8C	1053	0.5	1.9
LC 24-04 Pyroxene 9a	1058	1.1	4.2
LC 24-04 Pyroxene 9c	1054	0.6	2.3
LC 24-04 Pyroxene 9A	1066	2.2	8.3
LC 24-04 Pyroxene 9B	1059	1.2	4.7
LC 24-04 Pyroxene 9C	1052	0.4	1.5
LC 24-04 Pyroxene 10a	1050	0.1	0.4
LC 24-04 Pyroxene 10b	1057	1.0	3.7
LC 24-04 Pyroxene 10c	1054	0.7	2.6
LC 24-04 Pyroxene 10B	1058	1.2	4.6
LC 24-04 Pyroxene 10C	1054	0.6	2.3
LC 24-04 Pyroxene 1a	1038	1.2	3.9
LC 24-04 Pyroxene 1b	1039	1.3	3.9
LC 24-04 Pyroxene 1c	1031	0.2	3.9
LC 24-04 Pyroxene 1A	1060	3.5	4.0
LC 24-04 Pyroxene 1B	1063	3.9	4.0
LC 24-04 Pyroxene 1C	1061	3.7	4.0

LC 24-04 Pyroxene 7A	1025	-0.8	3.9
LC 24-04 Pyroxene 7B	1039	0.5	3.9
LC 24-04 Pyroxene 7C	1039	0.9	3.9

Appendix A-4. Pyroxene temperature and pressure data for Tumbres samples from Putirka et al., 2008.

Orthopyroxene and Clinopyroxene Temperature – Pressure – Depth Tumbres

Sample	Temperature (°C)	Pressure (kbar)	Depth (km)
LC 25-05 Pyroxene 1b	1090	1.2	4.6
LC 25-05 Pyroxene 1A	1086	0.7	2.8
LC 25-05 Pyroxene 3a	1094	1.7	6.4
LC 25-05 Pyroxene 3b	1092	1.4	5.3
LC 25-05 Pyroxene 3c	1099	2.3	8.8
LC 25-05 Pyroxene 3A	1083	0.3	1.2
LC 25-05 Pyroxene 3B	1096	1.9	7.2
LC 25-05 Pyroxene 3C	1090	1.2	4.7
LC 25-05 Pyroxene 6b	1095	1.8	6.9
LC 25-05 Pyroxene 6A	1090	1.2	4.7
LC 25-05 Pyroxene 6B	1087	0.8	3.0
LC 25-05 Pyroxene 6C	1091	1.3	5.1
LC 25-05 Pyroxene 10a	1088	1.0	3.6
LC 25-05 Pyroxene 10b	1090	1.2	4.7
LC 25-05 Pyroxene 10c	1097	2.1	8.1

LC 25-05 Pyroxene 10A	1100	2.5	9.5
LC 25-05 Pyroxene 10B	1089	1.0	3.9
LC 25-05 Pyroxene 10C	1093	1.6	6.0
LC 25-05 Pyroxene 2a	1088	2.4	8.9
LC 25-05 Pyroxene 2b	1093	3.1	11.7
LC 25-05 Pyroxene 2c	1102	3.6	13.6
LC 25-05 Pyroxene 2A	1093	3.3	12.6
LC 25-05 Pyroxene 2B	1092	3.1	11.6
LC 25-05 Pyroxene 2C	1087	2.4	9.2
LC 25-05 Pyroxene 4a	1087	2.7	10.1
LC 25-05 Pyroxene 4b	1085	2.6	9.6
LC 25-05 Pyroxene 4c	1066	0.0	0.1
LC 25-05 Pyroxene 4A	1127	5.9	22.3
LC 25-05 Pyroxene 4B	1097	2.8	10.6
LC 25-05 Pyroxene 4C	1094	2.7	10.1
LC 25-05 Pyroxene 5a	1080	1.7	6.6
LC 25-05 Pyroxene 5b	1080	2.0	7.5
LC 25-05 Pyroxene 5c	1088	2.6	9.9
LC 25-05 Pyroxene 5A	1080	1.8	6.7
LC 25-05 Pyroxene 5B	1082	2.2	8.3
LC 25-05 Pyroxene 5C	1090	2.8	10.6
LC 25-05 Pyroxene 7a	1082	1.9	7.4
LC 25-05 Pyroxene 7b	1071	1.0	4.0

LC 25-05 Pyroxene 7c	1054	-1.3	-5.1
LC 25-05 Pyroxene 7A	1075	0.8	2.9
LC 25-05 Pyroxene 7B	1086	2.8	10.4
LC 25-05 Pyroxene 7C	1075	1.5	5.7
LC 25-05 Pyroxene 8a	1078	0.3	1.2
LC 25-05 Pyroxene 8b	1056	-1.7	-6.3
LC 25-05 Pyroxene 8c	1119	2.3	8.9
LC 25-05 Pyroxene 8A	1094	2.8	10.7
LC 25-05 Pyroxene 8B	1080	2.0	7.6
LC 25-05 Pyroxene 8C	1092	2.9	10.9
LC 25-05 Pyroxene 9a	1083	2.4	9.0
LC 25-05 Pyroxene 9b	1106	4.7	17.7
LC 25-05 Pyroxene 9c	1099	4.0	15.1
LC 25-05 Pyroxene 9A	1082	2.0	7.6
LC 25-05 Pyroxene 9B	1089	2.3	8.6
LC 25-05 Pyroxene 9C	1099	3.0	11.2

Appendix B. Crystal maps for pyroxene, plagioclase, and full slide for all samples.

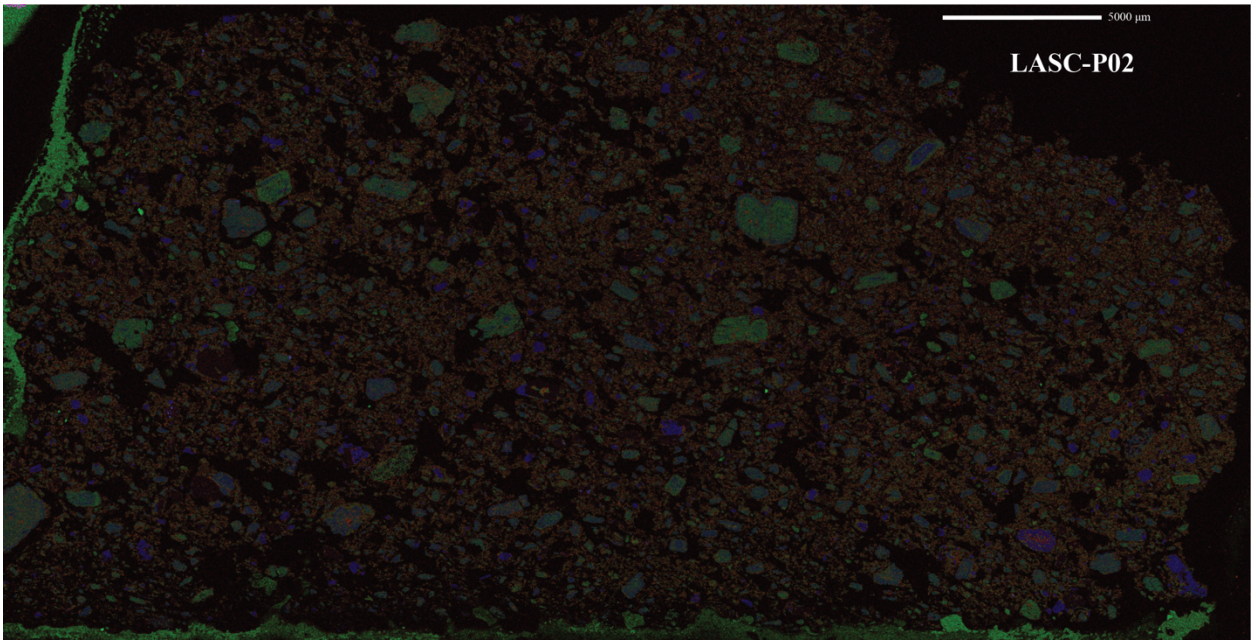

Chemical map of LASC-P02 slide.

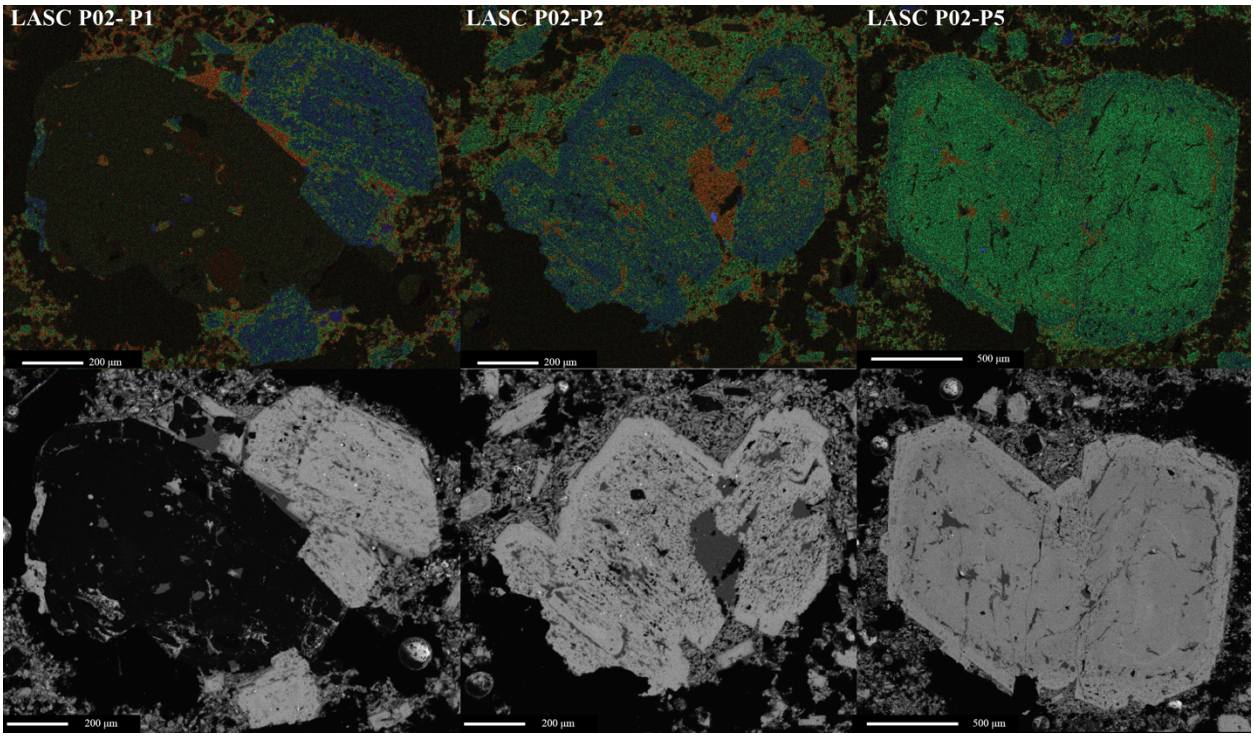

Chemical maps and Al element maps of LASC P02 crystals. Al maps are included to display textures.

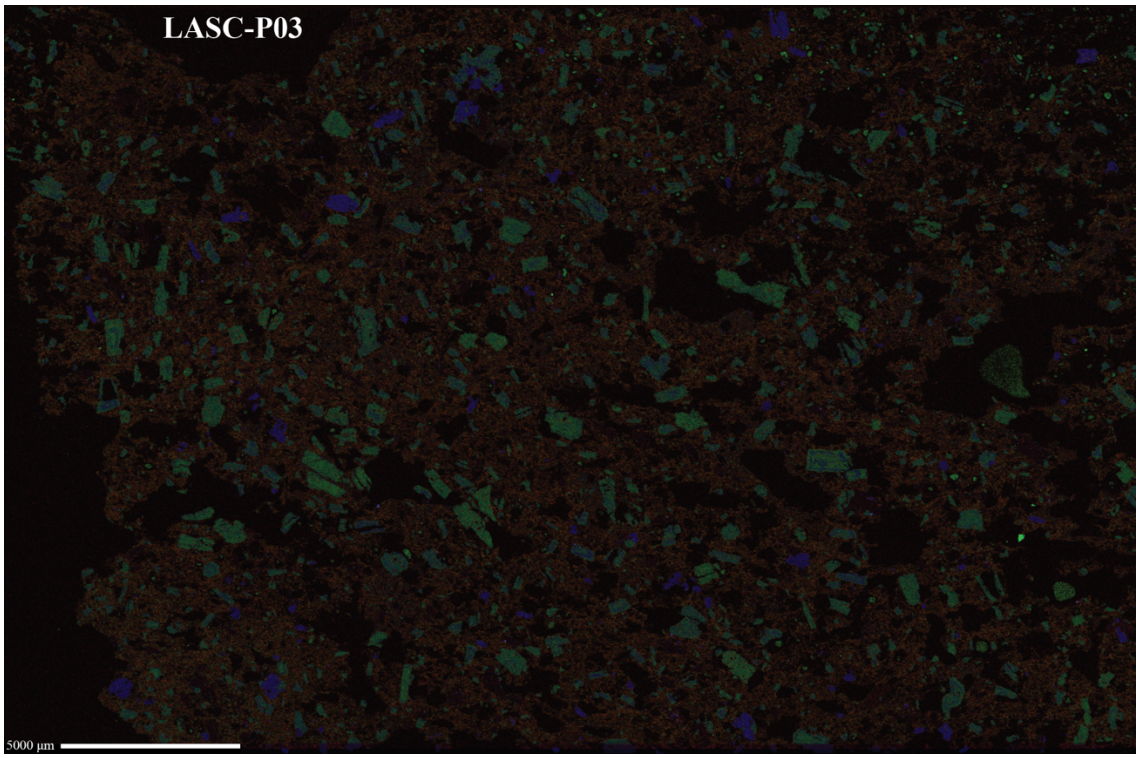

LASC-P03 chemical full slide map.

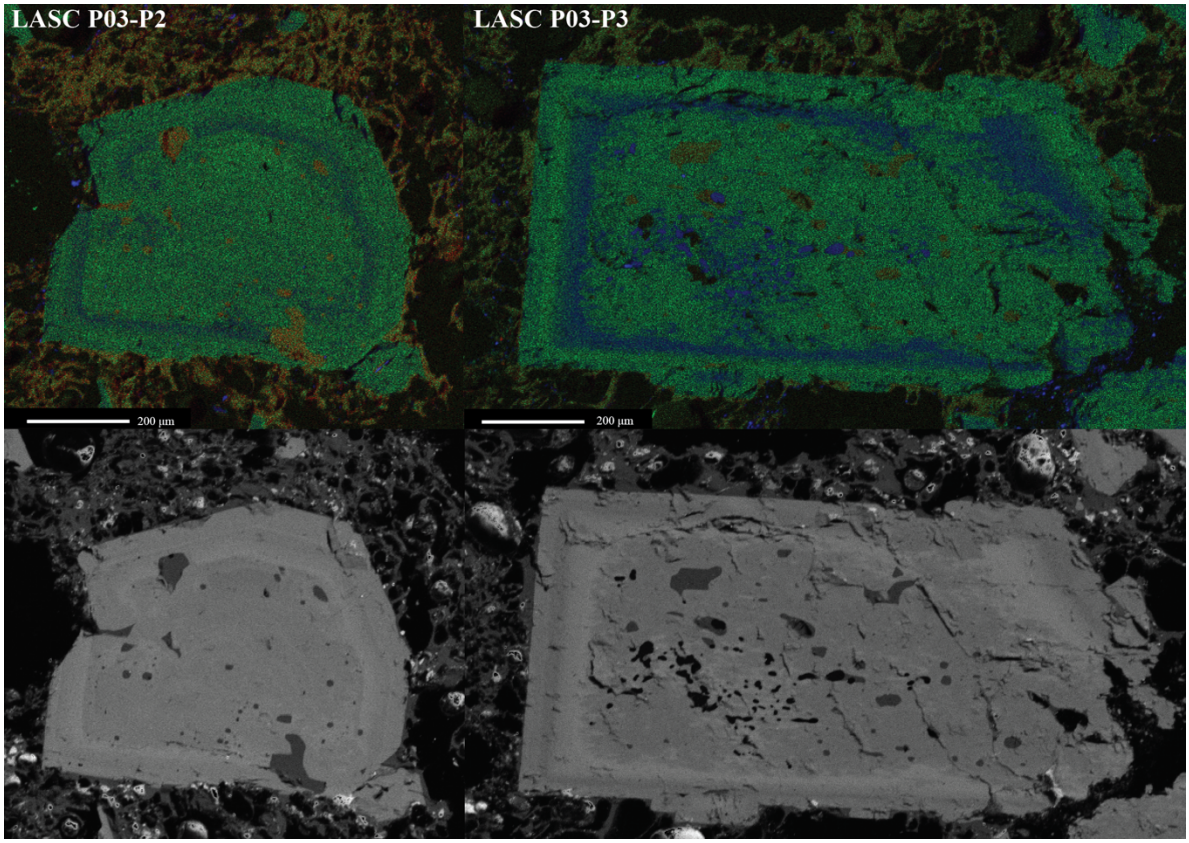

LASC-P03 crystals P2 and P2 chemical maps for K-Na-Ca and Al (bottom).

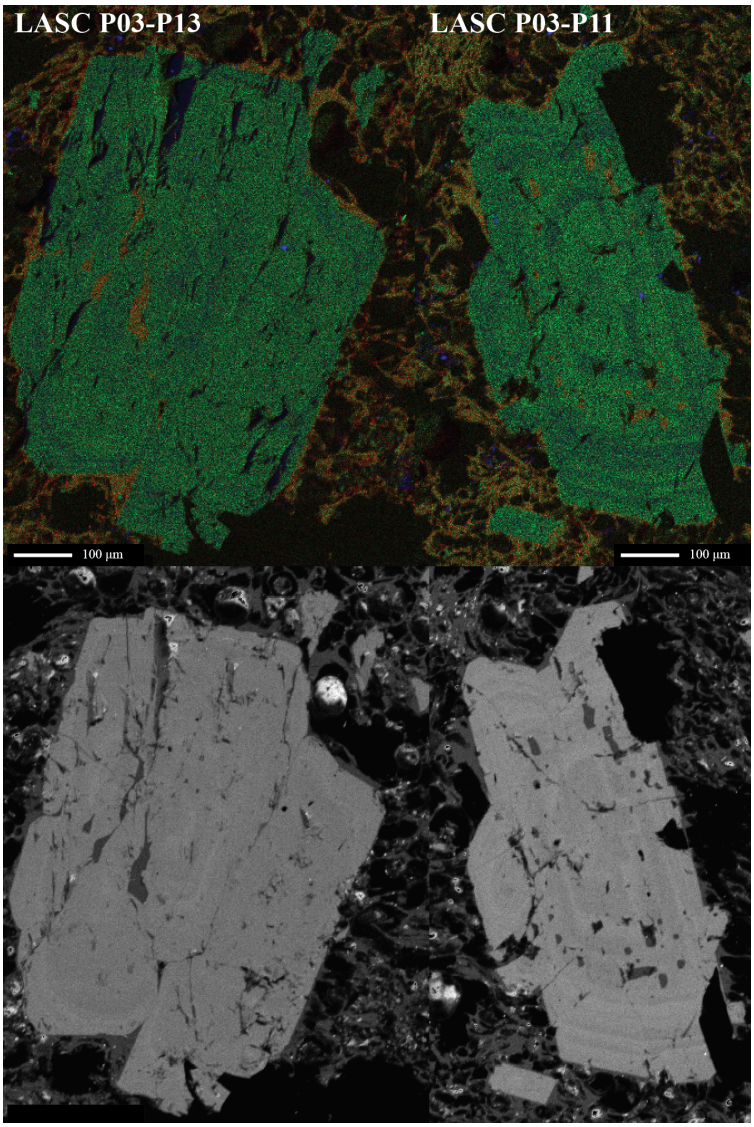

LASC-P03 crystals P11 and P13 K-Na-Ca and Al (bottom) chemical maps.

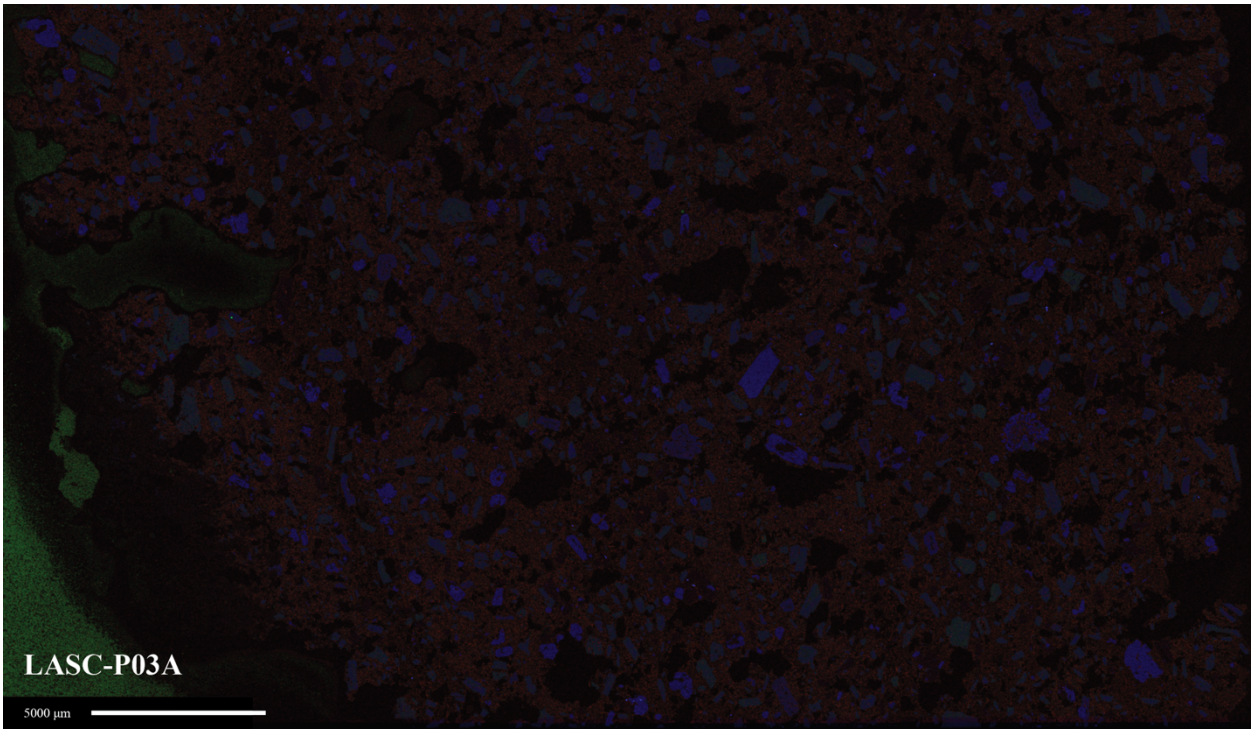

Chemical map of LASC-P03A.

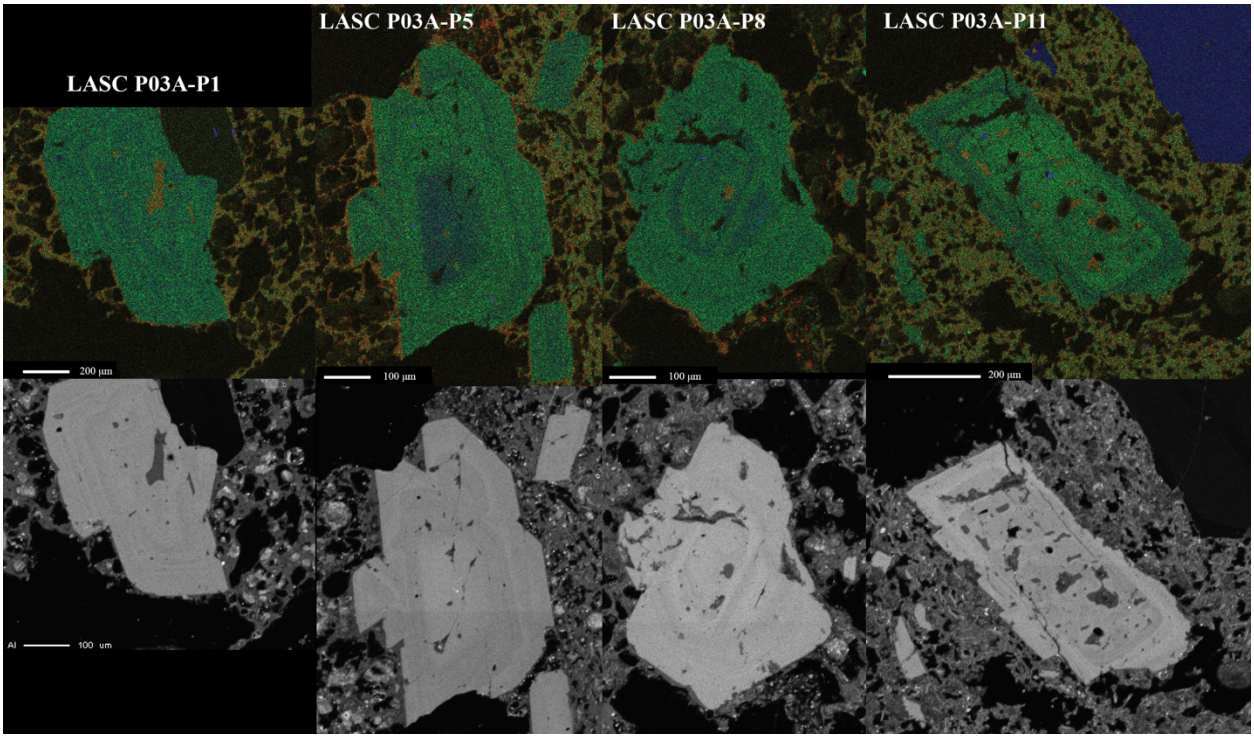

Plagioclase chemical maps from LASC P03A. Top are K-Na-Ca and bottom are Al.

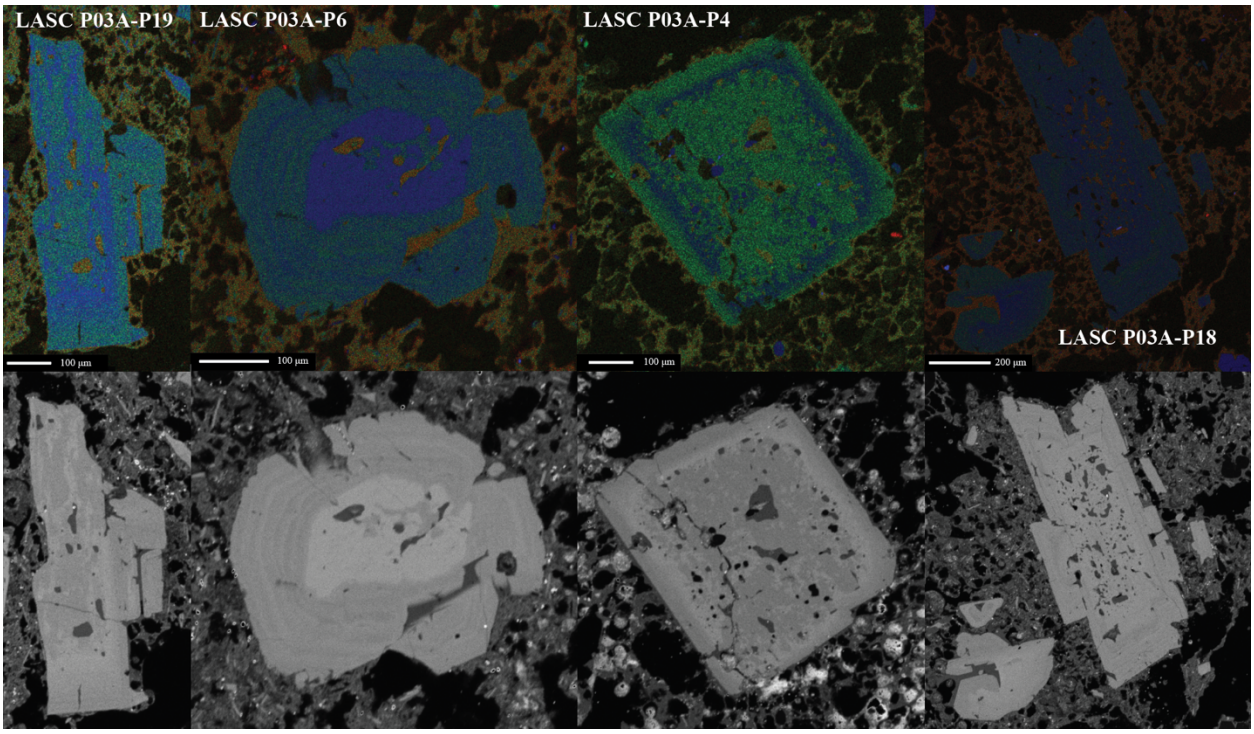

Plagioclase chemical maps from LASC P03A continued. Top are K-Na-Ca and bottom are Al.

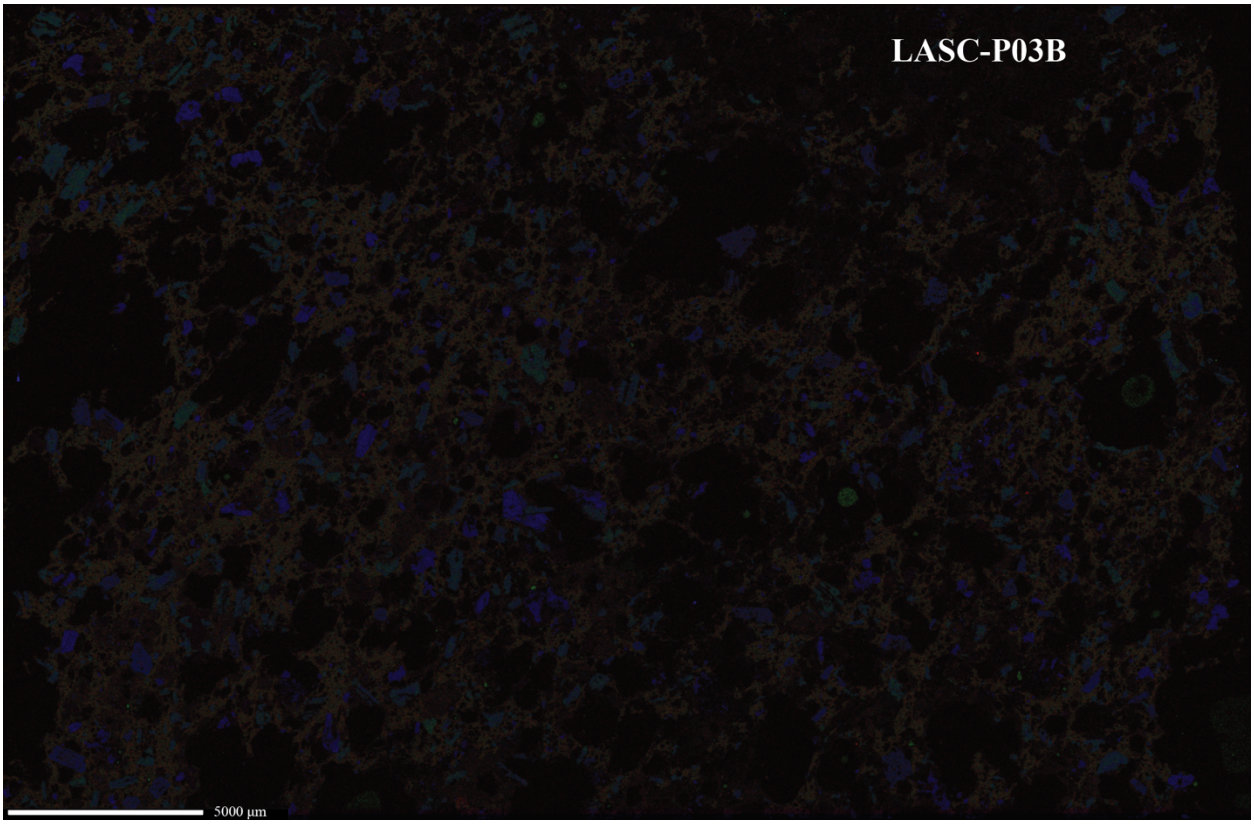

Chemical map of LASC-P03B.